

4 Protostellar cores in Sagittarius B2

5 NAZAR BUDAIEV ,¹ ADAM GINSBURG ,¹ DESMOND JEFF ,¹ CIRIACO GODDI ,^{2,3,4,5}
6 FANYI MENG ,^{6,7} ÁLVARO SÁNCHEZ-MONGE ,^{8,9} PETER SCHILKE ,⁷ ANIKA SCHMIEDEKE ,¹⁰ AND
7 TAEHWAA YOO 

8 ¹Department of Astronomy, University of Florida, P.O. Box 112055, Gainesville, FL 32611-2055, USA

9 ²Universidade de São Paulo, Instituto de Astronomia, Geofísica e Ciências Atmosféricas, Departamento de
10 Astronomia, São Paulo, SP 05508-090, Brazil

11 ³Dipartimento di Fisica, Università degli Studi di Cagliari, SP Monserrato-Sestu km 0.7, I-09042 Monserrato, Italy

12 ⁴INAF - Osservatorio Astronomico di Cagliari, via della Scienza 5, I-09047 Selargius (CA), Italy

13 ⁵INFN, Sezione di Cagliari, Cittadella Univ., I-09042 Monserrato (CA), Italy

14 ⁶University of Chinese Academy of Sciences, Beijing 100049, PR China

15 ⁷I. Physikalisches Institut der Universität zu Köln, Zülpicher Str. 77, 50937 Köln, Germany

16 ⁸Institut de Ciències de l'Espai (ICE, CSIC), Can Magrans s/n, E-08193, Bellaterra, Barcelona, Spain

17 ⁹Institut d'Estudis Espacials de Catalunya (IEEC), Barcelona, Spain

18 ¹⁰Green Bank Observatory, PO Box 2, Green Bank, WV 24944, USA

19 ABSTRACT

20 We present 500 AU and 700 AU resolution 1 mm and 3 mm ALMA observations,
21 respectively, of protostellar cores in the giant molecular cloud Sagittarius B2 (Sgr B2),
22 the most actively star forming cloud in our Galaxy. Previous lower resolution (5000
23 AU) 3 mm observations of this region detected \sim 150 sources inferred to be young stellar
24 objects (YSOs) with $M > 8 M_{\odot}$. With a tenfold increase in resolution, we detect 371
25 sources at 3 mm and 222 sources in the smaller field of view at 1 mm. The sources
26 seen at low resolution are observed to fragment into an average of two objects. About
27 a third of the observed sources fragment. Most of the sources we report are marginally
28 resolved and are at least partially optically thick. We determine that the observed
29 sources are most consistent with Stage 0/I YSOs, i.e., rotationally supported disks
30 with an active protostar and an envelope, that are warmer than those observed in the
31 solar neighborhood. We report source-counting-based inferred stellar mass and the
32 star formation rate of the cloud: $2300 M_{\odot}$, $0.0031 M_{\odot} \text{ yr}^{-1}$ for Sgr B2 N and $6300 M_{\odot}$,
33 $0.0085 M_{\odot} \text{ yr}^{-1}$ for Sgr B2 M.

34 1. INTRODUCTION

35 Many stars in our Galaxy were formed around
36 cosmic noon ($z \sim 2$, Madau & Dickinson 2014)
37 under conditions rarely seen today. To study

38 the conditions under which an average Galactic
39 star formed, we need to identify star-forming
40 regions which are analogous to those present
41 during cosmic noon. One such local environment
42 analogue is present in the high-density,
43 turbulent, and overall extreme Central Molecular
44 Zone (CMZ) (Henshaw et al. 2016). This

Corresponding author: Nazar Budaiev
nbudaiev@ufl.edu

is the only environment with such conditions where we can resolve disk scales (~ 100 s AU). The distribution of stellar masses, the initial mass function (IMF), is one outcome of star formation that may change under extreme gas conditions. In young star clusters near the center of the Galaxy, such as the Arches and Quintuplet, there is evidence of a top-heavy IMF (Hosek et al. 2019; Gallego-Calvente et al. 2022). By peering into early stages of star formation in the CMZ, we will investigate whether the IMF varies systematically with local environment and is thus shallower in the early universe. In this work, we examine the most actively star-forming cloud in the CMZ – Sagittarius B2 (Sgr B2).

The Galactic Center is located at a distance of 8.127 ± 0.031 kpc (GRAVITY Collaboration et al. 2018) and Sgr B2 is ~ 100 pc away from the Galactic Center in projection. Throughout this paper, we assume a distance to Sgr B2 of 8.4 kpc to remain consistent with the similar work by Ginsburg et al. (2018). The molecular cloud is split into several smaller, concentrated regions of star formation: North (N), Main (M), South (S), and Deep South (DS). A large fraction ($\sim 25\text{--}50\%$) of the current star formation in this cloud occurs in the N and M regions, with many stars forming in bound clusters (Ginsburg et al. 2018; Schmiedeke et al. 2016). Half of the total star formation in the CMZ occurs in Sgr B2, despite containing $\sim 10\%$ of the mass ($8 \times 10^6 M_\odot$) and $< 1\%$ of the volume (5×10^4 pc 3 ; Ginsburg et al. 2018; Barnes et al. 2017; Schmiedeke et al. 2016).

Sgr B2 appears to be forming stars preferentially in dense, bound clusters (Ginsburg et al. 2018; Ginsburg & Kruijssen 2018). Since other Galactic Center star clusters have excesses of high-mass stars (Hosek et al. 2019; Gallego-Calvente et al. 2022), Sgr B2 is likely also forming extra massive stars. 3500 AU resolution observations towards Sgr B2 N and M suggest the

presence of an excess of massive stars in the region (Sánchez-Monge et al. 2017). If this excess is present, it indicates a systematic variation of the stellar IMF with gas conditions, with a shallower IMF under conditions prevalent in galaxies with rapid star formation.

We report follow-up ALMA observations to ALMA project 2013.1.00269.S, which covered a 15×15 pc area around the Sgr B2 complex at 3 mm (Ginsburg et al. 2018) with ~ 5000 AU resolution. Our data covers Sgr B2 N and M at 3 mm and at 1 mm. We establish the possible nature and evolutionary stage of the sources. We place lower limits on cores' masses in the attempt to understand whether the IMF is top-heavy in young cluster and varies with the surrounding conditions.

In Section 2 we describe the observations and the imaging and self-calibration procedures. We then explain the source extraction approach in Section 3, make a comparison with previous low-resolution observations, and explain the way the spectral index was calculated between 3 mm and 1 mm. In Section 4 we show that our sources are consistent with Stage 0/I YSOs by ruling out other possible options. We also present calculations of the inferred stellar mass of the cloud and the star formation rate and present the multiplicity function. The paper is summarized in Section 5. In the appendices we briefly discuss the details of cleaning and self-calibration testing, radial core distribution for each protocluster, and show the fragmentation dependence on flux.

2. OBSERVATIONS AND DATA REDUCTION

This paper utilizes the data from ALMA Cycle 4 project 2016.1.00550.S. The observations consist of two pointings centered on Sgr B2 N (ICRS 17:47:19.925 -028.22.18.608) and Sgr B2 M (ICRS 17:47:20.174 -28.23.04.788) with the 12m antennas. Both locations were observed in Band 3 and Band 6 with resolution of $0.096'' \times$

131 0.073" (~ 700 AU) and $0.083'' \times 0.038''$ (~ 500
 132 AU), respectively. The pointings cover 6.5×4.5
 133 pc at 3 mm and roughly 1.75×3.75 pc at 1 mm
 134 out to primary beam level of 0.1. The spec-
 135 tral setup for each Band consists of 4 spectral
 136 windows with 1920 channels each and channel
 137 frequency width of 976.6 kHz (1.875 GHz band-
 138 width), which corresponds to spectral resolution
 139 of ~ 1.3 km/s at 226 GHz and ~ 3.2 km/s at 92
 140 GHz. The central spectral window frequencies
 141 are 217.84, 219.79, 231.80, and 233.67 GHz for
 142 Band 6 and 85.47, 87.37, 97.42, and 99.42 GHz
 143 for Band 3.

144 The data were imaged using CASA version
 145 5.7.0-134.el7 `tclean` with robust parameter set
 146 to 0.5 (McMullin et al. 2007). No line sub-
 147 traction or flagging was performed. Despite in
 148 the overlap between the Band 3 pointings, we
 149 used the standard griddler instead of the mosaic
 150 griddler. The initial cleaned images contained
 151 many imaging artifacts, such as radial streaks,
 152 circular patterns, and parallel “wavy” streaks.
 153 Therefore, we decided to self-calibrate the data
 154 to improve the quality of the final image. A
 155 detailed explanation of the tested approaches
 156 is presented in Appendix A. In summary, our
 157 standard self-calibration procedure consisted of
 158 the following steps:

- 159 1. Use one of the fully calibrated images
 160 from prior testing to estimate the low-
 161 est noise in the image. We measured the
 162 RMS in a box around an emission-free re-
 163 gion close to the center of the image.
- 164 2. Use the same previously cleaned image to
 165 create a “strict” contour mask at six- σ
 166 threshold.
- 167 3. Using the same image, draw a “broad”
 168 mask that covers all regions where signal
 169 is present, even if it includes some arti-
 170 facts or noise.
- 171 4. Clean the image with the `tclean` thresh-
 172 old parameter set to six times the noise

173 from step 1, and using the “strict” mask
 174 from step 2.

- 175 5. Complete a phase self-calibration with
 176 `solint` set to `inf`.
- 177 6. Repeat the clean from step 4.
- 178 7. Self-calibrate the image with `solint` set
 179 to `int`.
- 180 8. Clean the image with the `tclean` thresh-
 181 old parameter set to three times the noise
 182 from step 1 and using the “broad” mask
 183 from step 3.
- 184 9. Complete a round of phase and amplitude
 185 self-calibration with `solint` set to `inf`.
- 186 10. Repeat the clean from step 8.

187 However, some of the fields required further
 188 tuning to achieve better results. The Sgr B2 N
 189 Band 6 pointing suffered from divergence at the
 190 selected threshold values. Thus, we opted to in-
 191 crease the cleaning threshold up to ten times the
 192 noise until the amplitude self-calibration step
 193 was completed. After, we cleaned to three times
 194 the noise and added an extra amplitude and
 195 phase self-calibration step with `solint` set to
 196 15s, which we found to produce the best re-
 197 sults. The extra self-calibration step improved
 198 the image significantly. Running this extra self-
 199 calibration step on the other pointings did not
 200 reduce the noise in the images. The Sgr B2 N
 201 Band 3 pointing did not benefit from the am-
 202 plitude self-calibration step and introduced ad-
 203 ditional minor artifacts. Thus, we used the pre-
 204 amplitude-self-calibration image for our analy-
 205 sis. The final images for each Band are shown
 206 in Figures 1 and 2.

207 The final average RMS in an emission-free re-
 208 gion close to the center the image for each of the
 209 pointings is 0.033 mJy for N Band 3, 0.05 mJy
 210 for M Band 3, 0.35 mJy for N Band 6, and 0.25
 211 mJy for M Band 6. The RMS measurements for
 212 each calibration step are presented in Table 3.

Table 1. Summary of the observations.

Central frequency GHz	Date	$t_{science}$ seconds	Baseline length range meters	# of antennas
92.45	18-Sep-2017	2642	41-12100	43
92.45	18-Sep-2017	2644	41-12100	43
225.76	07-Sep-2017	2977	41-7600	46
225.76	16-Sep-2017	2973	41-12100	46

3. ANALYSIS

3.1. Source extraction

We strove to make the catalog as reproducible as possible, while minimizing the number of false positives. Automating source extraction presents numerous problems in a region like Sgr B2. The images have high dynamic range (~ 5000), contain complex extended structures, and like all interferometric single-pointing data, have radially varying noise. Combining this with the irregular structure of the observed objects makes fully automated source detection inefficient. Therefore, we utilized the automated source-finding dendrogram algorithm (Rosolowsky et al. 2008) augmented with a by-hand approach described below.

To avoid double counting sources we crop the overlapping parts of Band 3 imaged. The cut was made close to equidistant from the centers of the pointing, while not breaking up any regions with signal – just south of (below) H II region Sgr B2 Z10.24. Band 6 images do not overlap and thus do not require cropping. We divide each primary-beam corrected image in 30 concentric annuli and a circle at the center. We then use 7-sigma clipping to remove most of the signal from each of the annuli and calculate the standard deviation for each region. This noise measurement is then used as `astrodendro` input parameters.

The central part of the pointings are signal-dominated, which, even after sigma clipping, results in a higher measured noise. The calculated noise as a function of radius rapidly drops beyond the central clusters and then gradually

increases due to primary beam attenuation. We replace the estimated noise of the central part of the pointing with the lowest calculated value in the whole image such that the noise never decreases with radius.

Then, we perform source detection on the primary-beam-corrected images using the `astrodendro` source-finding algorithm. We generate a separate dendrogram for each concentric annulus using noise estimation for input parameters. We run the dendrogram on the full image and then exclude any sources with centers outside of the annulus. We set `min_value` to be equal to four times the noise estimate, `min_delta` to be 0.7 times the estimated noise, and `min_npix` to be 3 pixels.¹ The final source extraction thresholds are ~ 0.15 mJy at 3 mm and ~ 1.2 mJy at 1 mm within the inner 40% of the observed area, and ~ 0.5 mJy at 3 mm and ~ 4 mJy at 1 mm within the inner 90% of the imaged area. The exact values can be found in Table 3.

We then closely examine by eye parts of the image that contain extended structure and no compact emission, primarily H II regions. We draw polygons² around these locations by hand

¹ We tested a variety of combination of number of concentric annuli (10, 15, 20, 30), `min_value` (3σ , 4σ , 5σ), `min_delta` (0.5, 0.7, 1.0), and `min_npix` (2, 3, 5). We inspected each combination by hand to find a compromise between reducing the number of false positives due to artifacts and noise and increasing the number of likely positives.

² The polygon regions are available on GitHub with the rest of the reduction code: https://github.com/bazarsen/SgrB2_ALMA_continuum

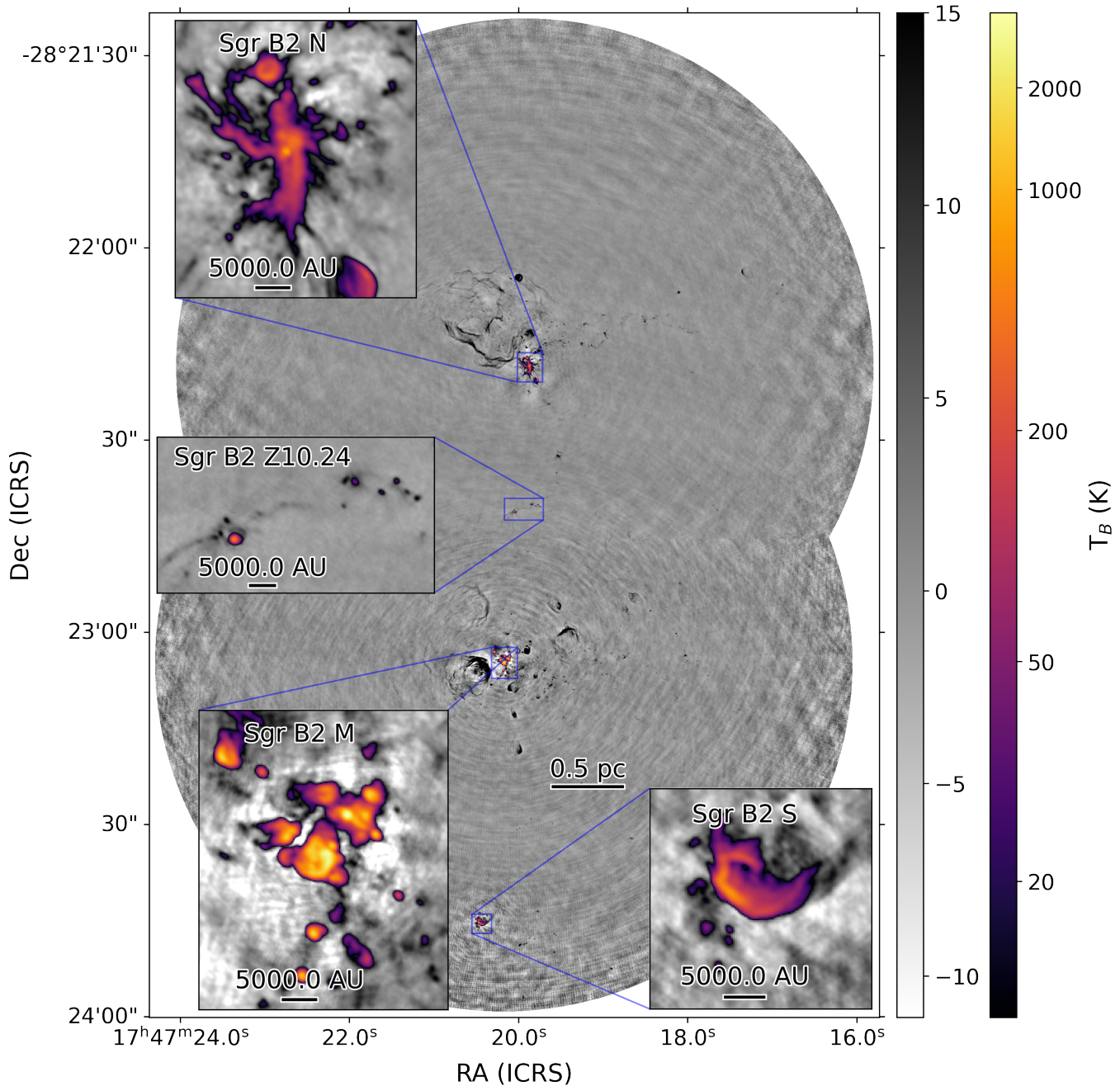


Figure 1. Band 3 (3 mm) continuum image of Sagittarius B2 N and M. The two pointings were imaged separately and then the final images were cut and overlaid to not overlap. The images were subsequently stitched together; the pixels in the central zoom-in come from only the N pointing. The insets show the high-density regions of Sgr B2 N and M, as well as Sgr B2 S and a region around H II region Sgr B2 Z10.24.

so that any detections within them can be excluded. In a few cases, we found core-like sources within the HII regions. We drew the polygons in a way that would include such sources in the final catalog.

Finally, we review each of the cataloged sources in both pointings and frequencies by hand. We rank every source as not-a-core (0), core candidate (1), or core (2). We inspect each source twice: first, zoomed-in closely to examine the shape and the background features and then using the whole image to get context on the source morphology based on location and proximity to other sources.

For example, if a source with a score of 1 that resembles a filamentary structure is located close to an area with extended emission, such as an HII region, we mark it as a false detection and adjust the score accordingly. If such a source is located in a cluster of other sources with a score of 2 and is not visibly a part of any extended structure, we change its score to 2. We further investigate each source with a score of 1 by comparing their structure in the 1 mm and 3 mm data. If a potential source is part of a filamentary structure at 3 mm, but no local peak is observed at 1 mm, we score such a source as a 0. Such a filamentary structure at 3 mm without a strong counterpart at 1 mm is indicative of free-free emission.

All of the extended HII regions are excluded manually using polygons as described above. In addition, we cross-match our detections with De Pree et al. (1998) and Meng et al. (2022) to remove known compact HII regions from our core sample and label them as known HII regions. We find that VLA-detected HII regions do not perfectly align with HII region candidates in our data, especially in Sgr B2 M. We attribute this to poor absolute pointing accuracy of the VLA (Mills et al. 2018). When it is not possible to establish a confident one-to-one match between catalogs we label the source

as an HII region candidate. Some of the previously known HII regions appear to have multiple peaks within their areas. We label these “fragmented” sources as HII region candidates.

To further indentify HII regions based on their spectral properties, we create a 1 mm to 3 mm spectral index map of the central, most dense parts of Sgr B2 N and M. We find that the central region of the Sgr B2 M, being more evolved compared to Sgr B2 N, has spectral indexes close to 0, which is typical for optically thin HII regions. Considering the high density of HII regions in the same area described in Schmiedeke et al. (2016) we mark all previously uncategorized sources in the close vicinity as HII region candidates and give them a score of 0. Only a few sources are removed in Sgr B2 N with this method due to the high error values of the spectral index map in the region. We label the sources morphologically resembles HII regions (e.g. a source with a dim center but bright edges) as HII region candidates. Finally, we mark sources that are extremely bright at 3 mm as HII region candidates. Every HII region candidate that is not a previously known HII region, cannot be assigned to a previosly known HII region accounting for VLA’s poor absolute pointing accuracy, and is not a part of a “fragmented” known HII region is marked as a new HII region detection. In total, our catalog contains 17 known hyper-compact and ultra-compact HII regions, 21 HII region candidates, and 8 new hyper-compact HII regions.

Having two criteria for core identification, strict and lax, allows for separate “robust” and “complete” catalogs to co-exist. We note that the difference between a score of 1 and 2 is subjective. After performing the analysis described in the following section, we do not find any significant differences when comparing the results between the two catalogs. Thus, we report and use only the “complete” catalog in the rest of this work. Our catalog contains 371 cores at 3

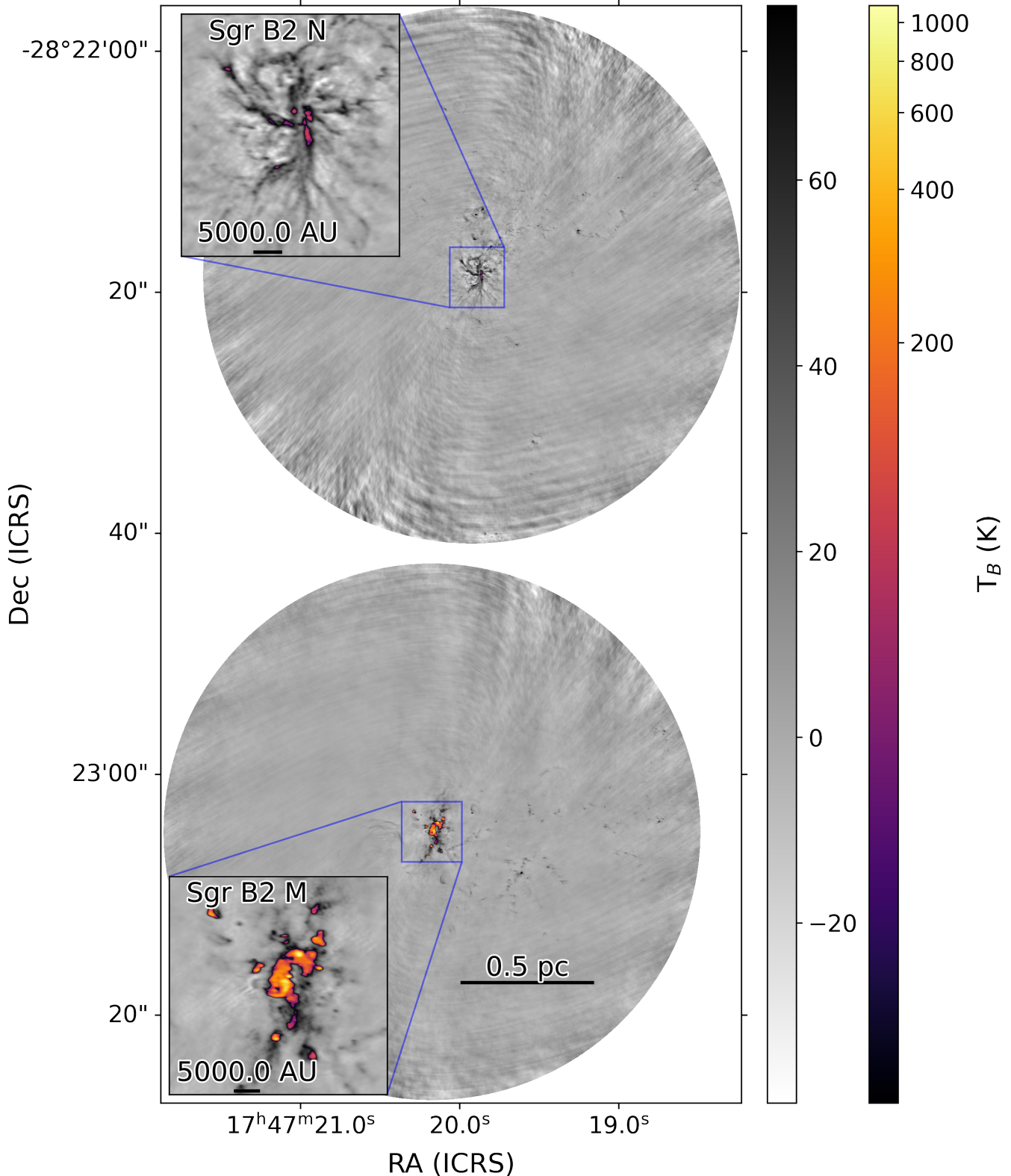


Figure 2. Band 6 (1 mm) continuum image of Sagittarius B2 N and M. Sgr B2 M appears to be hotter than Sgr B2 N. Due to the smaller field of view, HII regions Sgr B2 S and Z10.24 that are visible in Band 3 are not present here.

mm and 222 cores at 1 mm, of which 168 have a 3 mm counterpart. Thus, the total number of individual cores identified at at least one wavelength is 425.

The described approach has some caveats. Even after extensive self-calibration and cleaning, the data still include local artifacts such as negative bowls around bright sources and wave-like patterns on different scales. The high source density and the presence of extended emission (e.g. Figure 3), complicates the estimation of the local noise for each source.

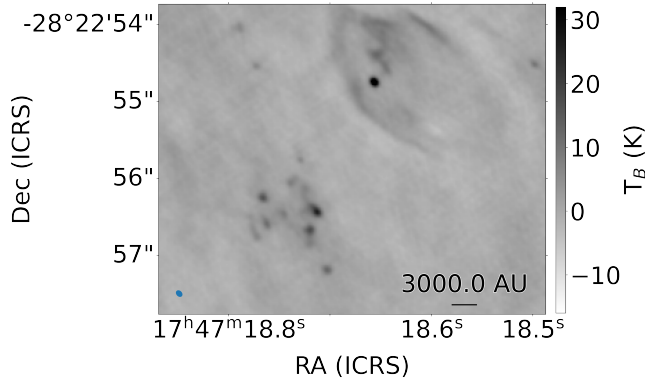


Figure 3. A zoom in on a region north-east from Sgr B2 M at 3 mm. It features H II region Sgr B2 Y from Schmiedeke et al. (2016) on the top-right, a core that is within the H II region’s projected area on the sky, and a highly-fragmented source on the bottom-left. This highly-fragmented group of ten detected cores was previously thought to be one massive core.

Excluding detections within polygons that were drawn by eye can potentially exclude true positives. While it is unlikely for cores to be present inside H II regions, they might appear to be so due to projection effects. Less than a few percent of the total pointing area is excluded by the polygons. Potentially missed sources should not affect the conclusions of this paper as there would be no biases for the excluded sources.

3.2. Photometry

We use the integrated flux within the dendrogram structure contour and the brightest pixel

within the contour as the primary observables. We present the two measurements of source flux in the catalog, a sample of which is shown in Table 4. The full catalog is available in machine-readable format. The source brightness temperatures are shown in Figure 4 as a cumulative distribution function (CDF). The total source flux is the sum of the pixel values in Jy in the dendrogram-defined contour referred to as a “leaf”. The peak is the value of the brightest pixel in Jy/beam. These numbers are expected to be the same for a point source and the peak-derived value should be smaller for a resolved source. Dendrogram-based flux underestimates the flux of the very faint sources because the lowest possible contour is set at a given threshold level, in our case 4σ .

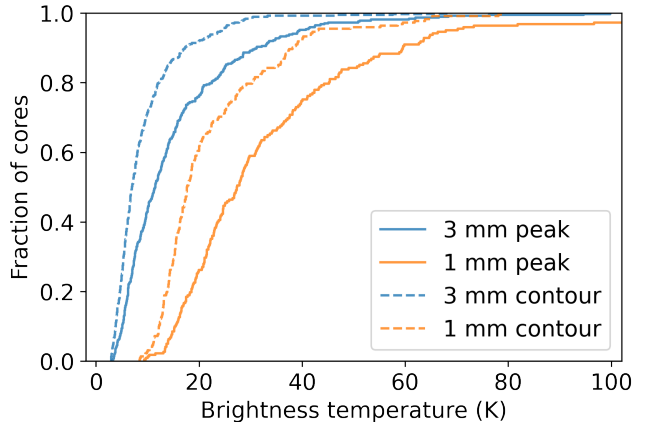


Figure 4. Brightness temperature of the catalogued cores. The brightness temperature is serves as a lower limit of the kinetic temperature for blackbody sources.

During testing, we attempted to perform 2D Gaussian photometry using the `gaussfit_catalog` python package. We inspected each fit by hand and found that fewer than 10% of the sources had a satisfactory fit for the central object. We found that many of the fits were affected by the presence of non-uniform extended envelopes around the centrally peaked sources, like in Figure 3. Furthermore, high source density and imaging artifacts also con-

tributed to some of the failed fits. Thus, we concluded that our sources are not well-represented by simple 2D Gaussians and decided to use dendrogram contours to define sources.

3.2.1. Photometry comparison

As a part of Cycle 4 ALMA project 2013.1.00269.S, [Ginsburg et al. \(2018\)](#), hereafter G18) obtained Band 3 observations of the extended Sgr B2 cloud at 0.5'' resolution.

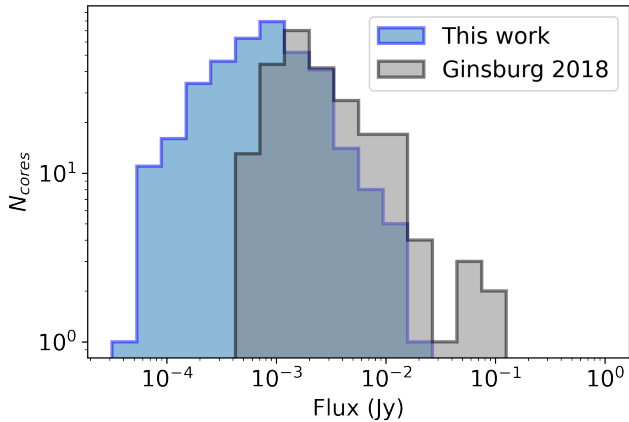


Figure 5. A comparison of our dendrogram contour-based, 3 mm source flux and the full 15×15 pc G18 catalog, with known H II regions removed from both data sets. The fluxes from G18 are divided by 0.92 to account for the difference in spectral setup assuming the sources have a spectral index of two. The general shape appears to be similar, but with the higher-resolution data, which have twice the sensitivity, we are able to detect fainter sources. The turnover point is at about 1 mJy, which is just below the turnover point in G18 catalog.

We investigate the impact of the differences between ours and G18 observations. Compared to G18, the catalog derived in this work has a factor of 10 better spatial resolution and is a factor of two more sensitive. The distribution of source fluxes is shown in Figure 5. The data from G18 were centered at 96.36 GHz with a bandwidth of 1.875 GHz, while our observations are centered at 92.45 GHz with the same

bandwidth. Since the central frequencies of the data are not the same, we perform a frequency correction. Assuming that the majority of the flux within the G18 beam is coming from the optically thick part of the core or an H II region and it has an average spectral index of two, the frequency correction factor is ∼0.92. For a positive spectral index, the flux measured from our data within the defined aperture is expected to be brighter. Depending on the source, the correction factor can range from 1.05 at spectral index of -1 to 0.87 at spectral index of 3.5 which would correspond to about 15% flux correction error. As shown in Section 3.4, many of the catalogued sources have spectral indexes between 2 and 3.

We compare our and G18 images by performing aperture photometry on G18 data. We apply an elliptical aperture equivalent to 1- σ of the G18 Gaussian beam ($0.230'' \times 0.197''$) on the locations of G18 detections on our data and compare it to the “peak” (brightest pixel) flux from G18. However, an elliptical aperture does not capture all the flux counted in the brightest pixel of an unresolved source. While the brightest pixel is representative of the sum of the Gaussian distribution of the signal, an elliptical aperture cuts off the edges of the distribution. We calculate the aperture correction factor as the fraction of the Gaussian distribution that is cut off after using a 1- σ -sized aperture to be 1.465. Finally, we convert the summed flux from Jy/beam to Jy. We compare this quantity with the brightest pixel of G18 sources. The ratio of flux at the location of each G18 source is shown in Figure 6. There is a slight trend of higher-resolution sources having less flux. A smaller fraction of sources are above the line. Low-flux sources exhibit larger scatter, which is consistent with measured noise. The somewhat large scatter can be partially explained by the presence of imaging artifacts in the images, primarily negative bowls.

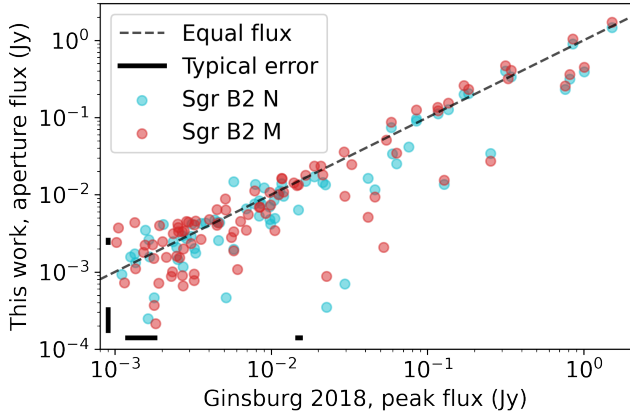


Figure 6. Aperture photometry comparison of our data and Ginsburg et al. (2018) data. The typical flux errors are shown as solid black lines at different fluxes on the log scale. Some scatter is present that can be explained by the difference in resolution, frequency, and the presence of imaging artifacts. The data points from Sgr B2 N and M that are almost identical are caused by the overlap in the two pointings’ field of view.

472

3.3. Source sizes

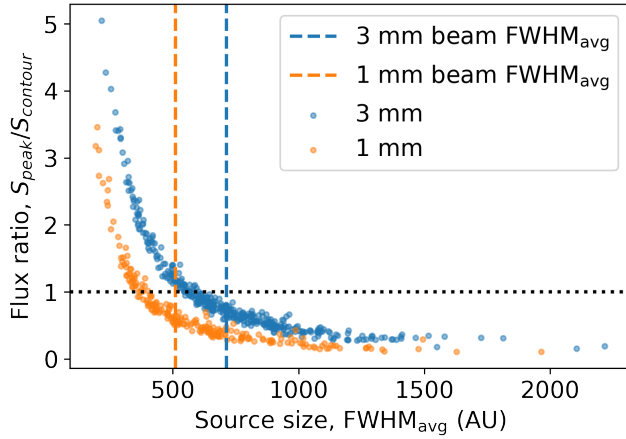


Figure 7. The ratio of the brightest pixel and the total source flux within dendrogram leaf structure is plotted against the average source FWHM as recorded by `astrodendro`. The flux ratios below one indicate likely resolved sources, which represent a majority in our sample.

473 For each source we recorded the total flux
474 within the dendrogram object contour and the
475 brightest pixel value within the contour. If a

476 source is not resolved, then the brightest pixel
477 should contain all the flux from the source. If a
478 source is resolved, the brightest pixel will con-
479 tain only part of the flux. Thus, we use a ratio
480 of brightest pixel flux and summed flux within
481 dendrogram structure to serve as a metric of
482 whether a source is resolved or not. As shown in
483 Figure 7, we find that 20% of 1 mm and 30% of
484 3 mm sources have effective areas smaller than
485 the beam area and peak flux larger than the
486 dendrogram contour flux, which means that the
487 sources are unresolved. On the other hand, only
488 a handful of sources are more than two reso-
489 lution elements across – 23 sources at 1 mm and
490 8 sources at 3 mm are well resolved.

491 The sources with $S_{\text{peak}}/S_{\text{contour}} < 1$ and den-
492 drogram contour area larger than the beam size
493 are marginally resolved. There are 45% of such
494 sources at each wavelength.

3.4. Spectral indexes

495 In order to measure the spectral indexes, we
496 need to convolve the data to a common beam.
497 The common beam between the two bands is
498 equivalent to the Band 3 beam. Thus, we con-
499 volve the Band 6 data to the Band 3 beam, ac-
500 counting for the beam area change as our data
501 are in units of Jy/beam. To calculate the spec-
502 tral index, we take the brightest pixel values for
503 detections at 3 mm and take the correspond-
504 ing positions on the sky at 1 mm. The bright-
505 est pixel contains information about at least the in-
506 nner, most dense part of the source in its 2D pro-
507 jection. The mean offset between the locations
508 of the brightest pixels at 3 mm and 1 mm is less
509 than a quarter of the beam, which is equivalent
510 to ~ 1 pixel and is never more than one common
511 beam apart. We find that using the 1 mm data’s
512 brightest pixel locations produces very similar
513 individual measurements, much less than the
514 calculated errors. We check for systematic er-
515 rors that could be caused by this approach and
516 find no trends in the measurements of the two
517 distribution. In addition to calculating spectral

519 indexes for sources present in both bands, we
 520 are also able to place upper and lower limits for
 521 sources detected only at 3 mm and 1 mm re-
 522 spectively. We show the distribution of spectral
 523 indexes with the corresponding source fluxes in
 524 Figure 8, indicating physical and observational
 525 constraints.

526 Since the flux measurements in two bands
 527 are uncorrelated distributions, we calculate the
 528 spectral index errors only for sources with SNR
 529 over 10 in both bands. For sources with SNR
 530 below 10 in either band, the errorbars are not
 531 necessarily representative of the uncertainty be-
 532 cause the error distribution function is no longer
 533 Gaussian (the distribution function for the ratio
 534 of two Gaussians with mean zero is a Cauchy
 535 distribution, for which the standard deviation
 536 and mean are undefined). We therefore show
 537 data points without error bars for these sources
 538 in Figure 8. All sources in our catalog have the
 539 $\text{SNR} > 4$.

540 Convoluting Band 6 data to the common beam
 541 results in a factor of two decrease in SNR
 542 for compact sources, which leaves only a few
 543 sources with SNR above 10 and significantly
 544 decreases the number of sources with $\text{SNR} >$
 545 4. Assuming that the radial brightness profile
 546 of the sources is the same, convoluting data to
 547 a larger beam would increase the source flux
 548 measurements by the same factor. The result-
 549 ing flux distribution of sources with the new,
 550 lower SNRs would be scaled, but have a similar
 551 shape. Thus, we use the original SNR, before
 552 data convolution, to perform the 10σ and 4σ
 553 cuts. We then use the convolved data to calcu-
 554 late individual source errors

555 We investigated whether we could use the
 556 alpha-maps produced by the `tclean` algorithm
 557 to estimate the in-band spectral indexes. Fewer
 558 than a dozen sources had errors below 50%.
 559 Thus, our data is not sensitive enough to pro-
 560 duce in-band spectral indexes.

561 We explore the potentially misclassified
 562 sources in our catalog. The “core” classification
 563 was done based on the morphology, proximity
 564 to other sources, relative brightness, and sur-
 565 rounding emission. The spectral index values
 566 can then be used to identify potential catalog
 567 contaminants such as H II regions. As shown in
 568 Figure 9, there are five sources that have sta-
 569 tistically significant spectral indexes below 2,
 570 which are probably misclassified H II regions.
 571 However, at least three of these sources are lo-
 572 cated in the negative bowls in Band 6 data.
 573 Since our cataloged fluxes are not background
 574 subtracted, being located in the negative bowl
 575 causes a lower 1 mm flux and underestimates
 576 the spectral index. Similarly, being located in
 577 a negative bowl at 3 mm artificially increases
 578 the spectral index. A known H II region Sgr
 579 B2 F10.30 is the most prominent example of a
 580 source in a 3 mm negative bowl, having $\alpha =$
 581 2.7. Thus, some of the detections near negative
 582 bowls might have been misclassified; as shown
 583 in Figure 8, there are some H II region candi-
 584 dates that have $\alpha > 2$ and cores with $\alpha < 2$.
 585 Fewer than 1% of sources are located in a vicin-
 586 ity of negative bowls.

587 We also note that just above 60% of our 3 mm
 588 detections fall within the field-of-view of 1 mm
 589 pointings. We extrapolate the derived spectral-
 590 index-based conclusions to the rest of the 3 mm
 591 sources. While the distance from the central
 592 regions of the clusters might have some impact
 593 on core temperature and age, it does not impact
 594 the conclusions of this paper.

596 3.5. Source masses

597 Using a number of assumptions about the
 598 properties of a core, including that the dust is
 599 optically thin, we can derive the mass of such a
 600 core. We start from a modified blackbody equa-
 601 tion:

$$F_\nu = \pi \frac{2h\nu^3}{c^2} (1 - e^{h\nu/k_B T})^{-1} (1 - e^{-\kappa_\nu \Sigma}), \quad (1)$$

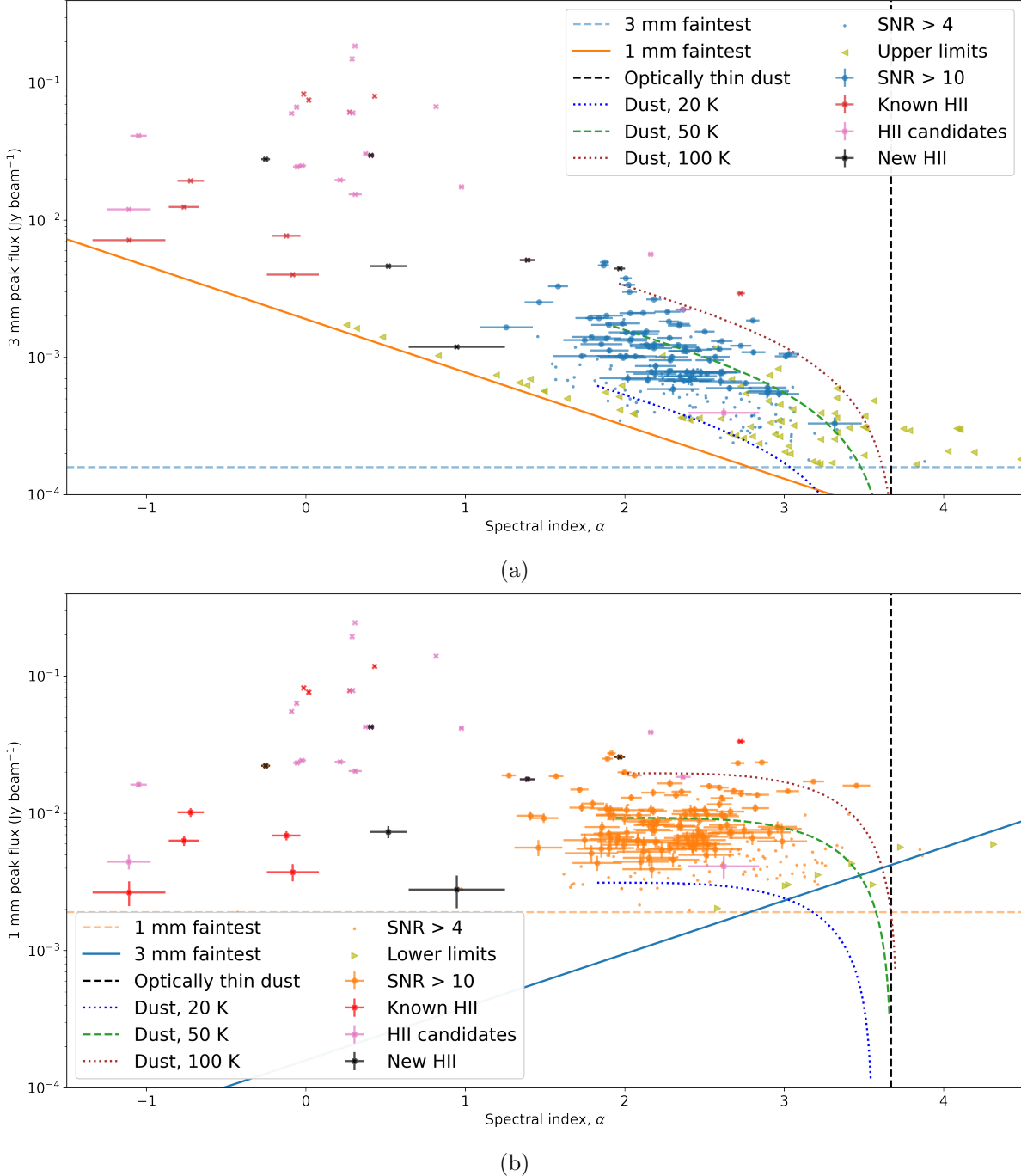


Figure 8. Source flux of 3 mm (a) and 1 mm (b) ALMA detections plotted against the calculated spectral index using the corresponding location at the other wavelength after matching beam sizes. Each line represents a physical or observational limit on possible values. We only calculate the errors of sources with signal-to-noise above 10, but all sources are shown for completeness. The 1 mm and 3 mm flux limits are based on the faintest detected source in the corresponding band. The dashed-green and dotted lines show the maximum flux at different temperatures of a source at different spectral indexes assuming the source is beam-sized. The detected sources fill the observable range completely. Follow up observations with higher sensitivities may reveal the missing dusty, optically thin sources. The olive triangles show the upper and lower limits on the spectral indexes for sources that have at least 4σ signal only in one band. The flux in the other band was taken as 4σ at that location in the image. The flux error bars are generally much smaller than the marker size and are only visible for low-flux sources.

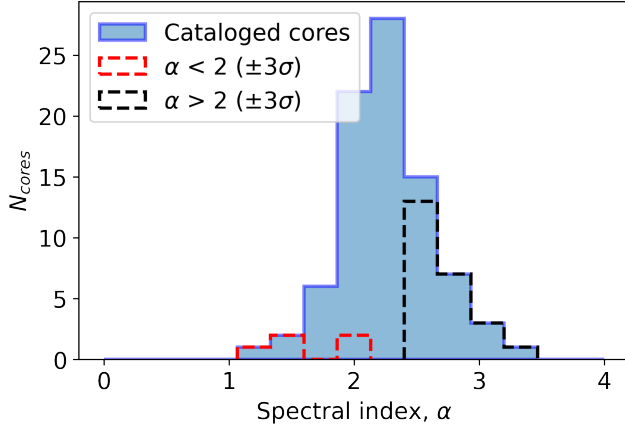


Figure 9. Spectral indexes of the sources in our catalog. We cross-matched 92.45 GHz and 225.78 GHz detections and calculated the spectral indexes as described in Section 3.4. We exclude any source that has the a continuum signal-to-noise below 10 in either band. The red dotted histogram shows the sources that have been cataloged as “cores” that have statistically significant ($\pm 3\sigma$) spectral index below 2. The black dotted histogram shows the fraction of sources that are not completely optically thick and have the calculated spectral index above 2.

where F_ν is the spectral flux density, h is the Planck constant, ν is the frequency, c is the speed of light, k_B is the Boltzmann constant, κ_ν is the dust opacity index, and Σ is the surface density. Given an area A , the mass M is

$$M = \Sigma A. \quad (2)$$

We can apply the optically thin dust assumption ($\kappa_\nu \Sigma \ll 1$) and solve for the mass:

$$M = \frac{S_\nu d^2}{B_\nu \kappa_\nu}, \quad (3)$$

where S_ν is the flux density, d is the distance to Sgr B2, and B_ν is the spectral brightness. Adopting the Rayleigh-Jeans approximation and expressing in terms of brightness temperature:

$$M = \frac{T_B d^2}{\kappa_\nu T_{KE}}, \quad (4)$$

where T_B is the brightness temperature and T_{KE} is the kinetic temperature of the source.

Extrapolating the Ossenkopf & Henning (1994) opacity models for dust grains with thin ice mantles, gas density of 10^6 cm^{-3} , and age of 10^5 years as a power law, assuming $\beta_{\text{dust}} = 1.75$, we obtain $\kappa_{92\text{GHz}} = 0.0017 \frac{\text{cm}^2}{\text{g}}$ and $\kappa_{226\text{GHz}} = 0.0083 \frac{\text{cm}^2}{\text{g}}$. Further assuming a uniform core temperature $T_{KE} = 50 \text{ K}$ and a distance³ of 8.4 kpc we obtain source masses shown in Figure 10.

Since the cores are at least partially optically thick, we can obtain only a lower limit on their dust masses. Other variables being constant, an optically thick source contains more mass than an optically thin source. Here, we utilize the

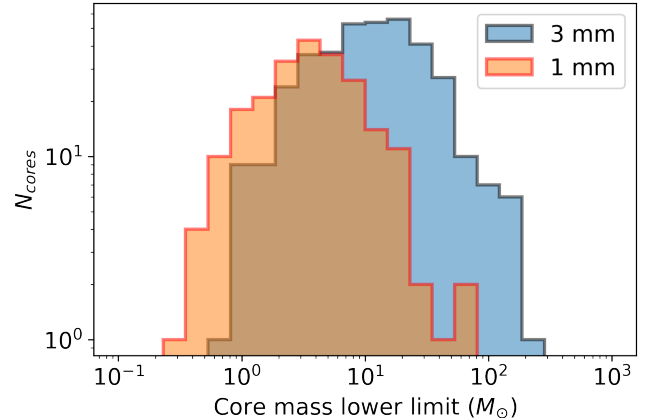


Figure 10. The inferred lower mass limit of the sources using the optically thin dust assumption for 1 mm and 3 mm data. 1 mm data has a higher mass sensitivity that is caused by the dust becoming more optically thick at higher frequencies and thus lower mass sources can be detected. We assume a uniform dust temperature of 50 K and a gas-to-dust ratio of 100. The turnover point at both wavelengths originates from the completeness limit over the whole imaged area.

total dendrogram flux instead of the source’s brightest pixel value to account for the sources that are partially resolved. Such a method

³ Using the most recently measured distance of 8.127 kpc (GRAVITY Collaboration et al. 2018) would result in 7% lower masses.

noticeably underestimates the masses of faint sources, as `astrodendro` algorithm cuts off every part of the source that is below 4σ .

Both the individual mass measurements and mass distributions based on the 1 mm and 3 mm observed flux do not match. We attribute this to the erroneous assumption of optically thin dust used for this calculation. Such an assumption underestimates the masses at 1 mm more than at 3 mm as dust has longer mean free path at longer wavelengths and thus flux is emitted from more of the material before reaching optically thick regime. Thus, we use the masses based on the 3 mm data as the lower limits in the rest of the paper. The core mass distributions have the turnover point at our completeness threshold over the whole imaged area.

Using 50 K uniform core temperature gives an understanding of possible mass ranges and shows the general shape of the core mass distribution. As shown by Bonfand et al. (2019), some cores can have average temperatures close to or above 150 K, usually referred to as hot cores. We detect sources at the locations of at least several such hot cores. Such sources are most likely the hot cores' central disks as our largest recoverable scale of ~ 7500 AU is on the lower side of the typical hot core sizes (Jeff et al., in prep.). At such high temperatures, the ice mantles surrounding the dust will start to sublimate. Such physical changes would decrease the emissivity by a factor of a few. We also do not expect a significant change to the gas-to-dust ratio based on freeze-out studies (Caselli et al. 2022).

4. DISCUSSION

4.1. Nature of the observed sources

4.1.1. Protostellar cores: Stage 0/I YSOs

Our “core” catalog consists primarily of compact dusty sources with sizes between 200 AU and 1000 AU. Based on basic modeling, we show in this section that our cores are most

consistent with an average temperature ~ 50 K. Such objects are, given the lower limit on their densities, unlikely to be in pressure equilibrium. We therefore identify these as rotationally-supported disks consistent with Stage 0/I YSOs⁴. We show the arguments in favor of this conclusion below.

In contrast to many studies of cores in nearby star-forming regions that assume a constant disk temperature of 20 K to make consistent comparisons between the works (e.g., Eisner et al. 2018; Otter et al. 2021) we show that the core temperatures in Sgr B2 are more consistent with $T = 50$ K. Average dust temperatures based on *Herschel* line-of-sight observations (Etxaluze et al. 2013) and theoretical models of external dust heating due to stars (Schmiedeke et al. 2016) both produce ~ 20 K average temperature in the moderate-density dust ($n \lesssim 10^5$ cm $^{-3}$) in Sgr B2 region. However, the denser regions have gas temperatures that are substantially higher (e.g., Ginsburg et al. 2016; Krieger et al. 2017). The modeled dust temperatures towards the centers of Sgr B2 N and M can go as high as 350 K and 600 K respectively (Schmiedeke et al. 2016). Since we are observing cores, which are local overdensities, we expect temperatures higher than 20 K.

If we assume, very simplistically, that all of our observed cores are optically thick beam-sized spheres, about 50% of the cores at 3 mm and fewer than 20% of the cores at 1 mm are consistent with temperatures below 20 K, as shown in Figure 11. In reality, it is extremely unlikely that all of the cores are close to beam-sized. Sources smaller than the beam size would need to be warmer to produce the same flux. Furthermore, Figure 8 shows that most of the cores are not completely optically thick, which

⁴ We extrapolate the original luminosity-accretion-based definition of stages for low-mass sources to their high-mass analogues from Robitaille et al. (2006).

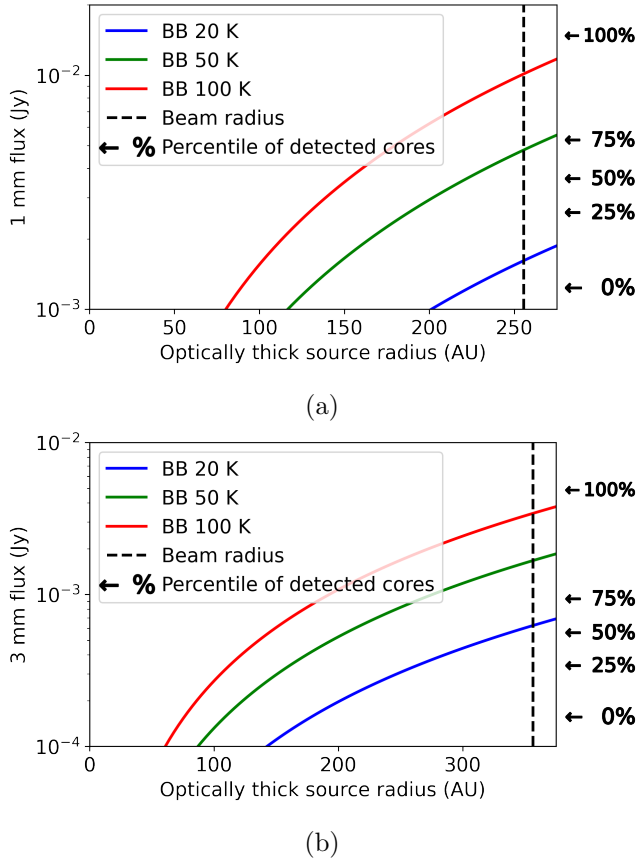


Figure 11. A model of an optically thick (blackbody) source within our beam at 1 mm (a) and 3 mm (b). By changing the size of the optically thick sphere we can see how many of the sources in our core catalog can be explained using this model. Assuming a beam-sized or larger optically thick core, less than 20% of the 1 mm detections can be explained by core temperatures of 20 K. If some of the sources are smaller and are not completely optically thick, the average temperature would have to be even higher. Thus, we assume a higher average core temperature of 50 K.

requires the assumed temperatures to be even higher. About 75% of 1 mm detections are consistent with average temperatures of at least 50 K with the remaining 25% being hotter. Thus, in this work we take the average core temperature to be 50 K.

To test our assumptions, we create a simple model of our observed sources. It consists of an optically thick sphere of radius R that is surrounded by optically thin dust of a certain

surface density. This model mimics a face-on optically thick disk embedded in dust and is intended to confirm that we are able to detect dusty disks. Since many of our sources are calculated to be slightly optically thick, we also use this to test the expected spectral indexes for optically thick sources embedded in optically thin dust.

Assuming a gas-to-dust ratio of 100, we represent the dust surface density using gas column density, with an average over the Sgr B2 N and M cluster of around $3 \times 10^{24} \text{ cm}^{-2}$ (Sánchez-Monge et al. 2017). As discussed above, we assume a dust temperature of 50 K. Figure 12 shows the expected spectral indexes of such sources as a function of the radius of the central optically thick sphere and the gas surface number density. We further indicate the region on the plot that will not be detectable in either of our bands at our sensitivity as the white-out region on the bottom left. The unshaded region of the plot corresponds to the parameters of our simplified model that can explain the observed sources.

Using this model, for an optically thick face-on disk with an average temperature of 50 K we conclude that: a) in lower column density regions ($< 10^{24} \text{ cm}^{-2}$) we are sensitive to sources that are larger than $\sim 300 \text{ AU}$ in diameter and b) as the density increases past the average density in Sgr B2 (and up to 10^{26} cm^{-2} where the surrounding dust becomes optically thick) the optically thin dust becomes the dominant source of emission.

The sources in our catalog are also much brighter than in any of the nearby star-forming regions. In the Orion molecular cloud only four of the brightest disks would be detectable at Sgr B2's distance (Tobin et al. 2020). Only a few of the disks in Orion are larger than 200 AU with corresponding masses of $0.2 M_{\odot}$. The sources in our catalog are most likely larger, more massive, and warmer than the ones in Orion.

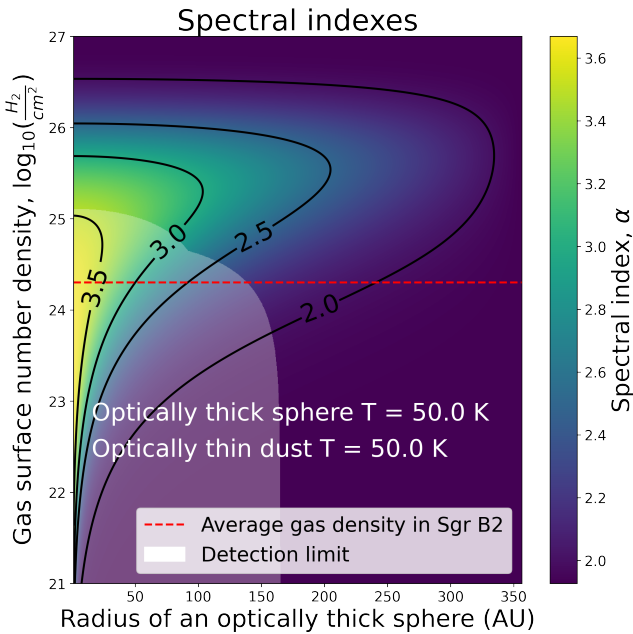


Figure 12. Modeled spectral indexes for an optically thick spherical core of a certain radius surrounded by optically thin isotropic dust of a given gas surface number density. A gas-to-dust ratio of 100 is assumed. The average gas surface density of $3 \times 10^{24} \text{ cm}^{-2}$ in Sgr B2 (Sánchez-Monge et al. 2017) is most likely representative of the minimum gas surface density within our beam centered on our detections. We do not expect any sources to be below this line, since all detections represent overdensities. At gas surface densities of $\sim 4 \times 10^{26} \text{ cm}^{-2}$ the dust surrounding the central sphere becomes optically thick. The spectral index of an optically thick blackbody at 50 K is close to 1.93. The white shaded area indicates a parameter space of sources below our data's sensitivity.

4.1.2. H II regions

We evaluate whether the sources with $\alpha \approx 2$ could be H II regions and conclude that they are most likely not. At brightness temperatures of 10^4 K , in order to match the range of recorded fluxes in our catalog, an optically thick H II region would have to be between 30 AU and 80 AU in diameter. Using a Strömgren sphere as an approximation, we know that:

$$Q(H^0) = \frac{4}{3}\pi R^3 N(H)^2 \alpha_B, \quad (5)$$

where $Q(H^0)$ is the number of ionizing photons, R is the radius of the ionized sphere, $N(H)$ is hydrogen number density, and α_B is the recombination rate to all levels excluding the ground level, $\approx 4 \times 10^{-19}$. Taking $Q(H^0)$ between $5 \times 10^{47} \text{ s}^{-1}$ and $1.5 \times 10^{49} \text{ s}^{-1}$, equivalent to B0-O6 stars, we find that 30-80 AU, hyper-compact H II regions can potentially exist in densities between 10^7 and 10^9 cm^{-3} . These densities are reasonable for Sgr B2 (Meng et al. 2022). However, any optically thick H II region larger than 80 AU in diameter should be detected with our sensitivity. No such sources are present in our catalog. Roughly 100 sources in our catalog have $\alpha \approx 2$. By making several assumptions, such as higher H II region metallicity (which will lower its electron temperature) and the right amount of high-mass stars embedded in higher-than-previously-measured gas densities, many of the observed optically thick sources can be attributed to 30-80 AU H II regions. At the same time, there exists a population of H II regions larger than 500 AU (e.g. this work, Meng et al. 2022). Assuming that the H II regions evolve continuously, the absence of 80-500 AU scale H II regions indicate that there was an abrupt period with no stars being formed. A short, temporary, and complete interruption of star-forming processes would be extremely unusual. Thus, we claim that there are very few to none H II regions contaminating our catalog. Additional observations, e.g. radio recombination lines, could help determine the nature of these sources definitively.

4.1.3. Prestellar cores

As described in Section 3.5, we can place a lower limit on the masses of our sources by assuming each is a beam-sized uniform sphere with a dust optical depth of 1. Free-fall time of a spherically-symmetric core is:

$$t_{ff} = \sqrt{\frac{3\pi}{32G\rho}} = \sqrt{\frac{3\pi V}{32Gm}} = \sqrt{\frac{\pi^2 R^3}{8Gm}}, \quad (6)$$

where G is the gravitational constant and V , m , and R are the volume, mass, and radius of a core. Taking the least massive source in our catalog ($\sim 1 M_{\odot}$) to be beam-sized (~ 700 AU) would result in free-fall times of 1200 years, while the most massive core of the same size would have a free-fall time of 40 years – extremely short on star formation scales. Thus, it is unlikely that any of our sources (at least on ~ 700 AU scales) are still undergoing free-fall collapse, indicating that there are no prestellar cores in our sample. While this is an extreme approximation, the higher mass, heterogeneous nature of the source, and the influence of the surrounding environment would speed up the infall of the material.

We can further estimate the effects of the high-pressure environment using the Bonnor-Ebert mass:

$$M_{BE} = 1.18 \frac{c_s^4}{G^{3/2} p_{BE}^{1/2}}, \quad (7)$$

where c_s is the speed of sound, 0.4 km/s ($T = 50$ K), G is the gravitational constant, and p_{BE} is the pressure ($P/k_B = 10^8 - 10^{13}$ K cm $^{-3}$ (Myers et al. 2022)). The maximum Bonnor-Ebert mass for the sources in Sgr B2 is then $\sim 1 - 1 \times 10^{-3} M_{\odot}$. Only two cores in our catalog have mass lower limits below $1 M_{\odot}$. Thus, the majority of the cores are not pressure supported. Having ruled out the free-fall collapse and pressure support, and the improbable magnetic field support, the remaining option is the rotational support of disks.

4.1.4. Stage II and III YSOs

With a dust mass lower limit of the catalogued sources, we can approximate the masses of the central stars for Stage II YSOs. We extrapolate the ratio of the dust mass and the central star of $\sim 1\%$ (Williams & Cieza 2011) one order of magnitude for more massive objects to calculate the possible mass of the central star for the least massive sources in our catalog. The

faintest source in our data is 1.2 mJy at 1.3 mm, which would correspond to a central star with a mass of at least $30 M_{\odot}$. If all of our observed sources are Stage II YSOs, the median star mass would be around $300 M_{\odot}$, which is on the order of the largest stars ever detected. Current disk demographic samples (e.g., Andrews et al. 2018; Williams & Cieza 2011) are limited to $M \lesssim 2 M_{\odot}$. Finally, if we assume an optically thick, face-on dusty disk with an average temperature of 50 K, the disk would have to be at least 200 AU in size to be detectable with our sensitivity. All of our targets, if they are disks, must be larger and more massive than any disks observed in the local neighborhood (e.g., Andrews et al. 2018). Stage III YSOs do not have infrared excess and thus could not possibly be detected in our data.

4.2. Inferred stellar mass

We augment the method described in G18 to calculate the inferred stellar mass for each cluster. We use the core mass calculations from Section 3.5 to calculate the potential stellar mass assuming that roughly one third of a core mass will end up in a star (Lada & Lada 2003). We take 6σ as our completeness limit within the cluster boundaries – 0.3 mJy for Sgr B2 M and 0.2 mJy for Sgr B2 N, which corresponds to $1.5 M_{\odot}$ and $1 M_{\odot}$ stellar mass respectively. We exclude all the sources below this completeness limit. Following the clusters' extent used in Schmiedeke et al. (2016) and G18, we take the radii of Sgr B2 N and M clusters to be 0.4 pc and 0.5 pc, respectively. We then assume that each HII region is powered by a $> 20 M_{\odot}$ star. We count the number of HII regions within each cluster from De Pree et al. (1998) and Meng et al. (2022). We assume a Kroupa initial mass function (Kroupa 2001) to perform the following estimates. The average mass of the stars powering the HII regions is $45 M_{\odot}$. Combining the core-based stellar mass with the HII region-based stellar mass we infer

the total stellar mass by extrapolating for the stars below our completeness limit. Following the arguments outlined in G18, we estimate the star formation rate (SFR) for each cluster, taking the age of the cloud as 0.74 Myr (Kruijssen et al. 2015). The results and comparison with previous works are shown in Table 2.

With the high-resolution data, it is evident that the historically defined sizes of Sgr B2 Main and North in Goldsmith et al. (1990) do not necessarily represent which sources are part of the clusters. Both N and M have a continuous “chain” of sources in projection in the eastward direction, as visible in Figures 1 and 2. The defined sizes cut through these “chains” of sources. Further kinematics studies of the region that extended beyond the centers of the clusters (e.g. Schwörer et al. 2019) are needed to determine which sources belong to which protocluster and would allow for more accurate count-based cluster mass estimation.

We use the variability of inferred total stellar mass as a function of assumed catalog mass completeness limit, like shown in Figure 13, to make a conjecture on the shape of the IMF. Let an observed cluster have a Kroupa IMF. Assuming that the observationally-derived masses match the actual masses of the cores, as long as we choose an assumed completeness above the “true” completeness, the Kroupa-IMF-based total inferred stellar mass will remain the same. This would show up as a horizontal line on Figure 13. If we pick a mass completeness limit below the “true” completeness, we will underestimate the total mass.

Now, assume that the observed cluster has a high-mass star excess (i.e. shallower IMF). If we repeat the same exact process of inferring the total stellar mass assuming a “normal” Kroupa IMF, we will consistently overestimate the total mass. Moreover, the larger the assumed completeness limit we choose, the more the mass will be overestimated. This would correspond

to a line with an upward trend on Figure 13. The inferred stellar mass as a function of assumed completeness limit for this work appears to have such an upward trend, which could be indicative of a shallower IMF.

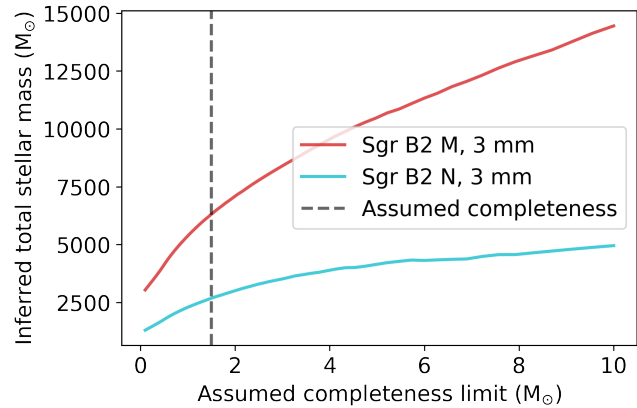


Figure 13. Inferred total stellar mass for Sgr B2 N and M as a function of the assumed completeness mass limit in our data. The assumed completeness for the calculations shown in Table 2 is taken at 6σ and converted to star mass equivalent assuming optically thin dust and a 30% star formation efficiency and is shown as a dashed line.

4.3. Core fragmentation

We compare our core catalog with G18, which observed Sgr B2 N and M at 10 times coarser resolution. For each low-resolution detection, we find the number of high-resolution detections within $1.5 \times$ beam FWHM of the source center. We exclude sources from the G18 catalog that would not be detectable in our data, specifically at the pointing edges where the sensitivity is lower. Out of 371 detections at 3 mm in our catalog, 109 cores are contained within the fragmented low-resolution sources, 42 are one-to-one match, and the remaining 220 are new detections with no corresponding detections in G18.

Our shortest baseline length of 41 m is longer than the 15 m in G18 data. On average, our images are made weighting longer baselines. As

Table 2. Inferred stellar mass of Sgr B2 N and M using source counting. Using the calculated core mass, we estimate the core-based stellar mass (M_{count}). We assume a lower completeness limit to be $1.5 M_{\odot}$ in stellar mass and use Kroupa IMF (Kroupa 2001) to infer the stellar mass ($M_{inferred,core}$). We assume that each H II region contains a $45 M_{\odot}$ star to infer the $M > 20 M_{\odot}$ tail of the IMF. Combining the direct counting of cores and H II regions, we infer the total stellar mass in each cluster ($M_{inferred,total}$). The star formation rate assumes $t_{SF} = 0.74$ Myr.

Name	M_{count} (M_{\odot})		$M_{inferred,core}$ (M_{\odot})		$M_{inferred,total}$ (M_{\odot})		SFR ($M_{\odot} \text{ yr}^{-1}$)	
	This work	G18	This work	G18	This work	G18	S16	
N	960	270	5900	1500	2300	1200	2400	0.0031
M	490	2300	5100	2300	6300	8800	20700	0.0085

the result, some of the previous detections can be resolved out. We find that over a dozen sources from the low-resolution catalog do not have a counterpart in the high-resolution catalog. The high-resolution data's largest recoverable scale is $0.9''$, or ~ 7500 AU. While some faint and extended sources might indeed have been resolved out, at least some of the low-resolution detections are likely false positives due to imaging artifacts.

We find that over half of the low resolution detections “fragment” into two or more sources, with one of the sources fragmenting into ten, as shown in Figure 3. The distribution is shown in Figure 14. We do not find any pattern in the locations of the cores that fragment vs those that do not. Figure 15 shows the spatial distribution of the cross-matched and resolved-out sources as well as the new detections.

On average, each detected G18 source fragments into 2 cores. If we take the one third of the sources that fragment, then there is an average of 3.4 cores per G18 fragmenting source. In general, source fragmentation changes the shape of the core mass function (and if these fragments represent individual systems – the IMF), making it less steep. Because cores previously inferred to contain single, very massive star are broken into many lower-mass objects, increasing the total number of sources, the total expected luminosity reduces significantly.

We find that any source from G18's catalog, at 5000 AU resolution, with flux above 20 mJy ended up being fragmented at 700 AU resolution. It is not possible to place meaningful lower limits on the fragmentation function at low flux: the sources are more likely to be close to the sensitivity limit of the higher-resolution data.

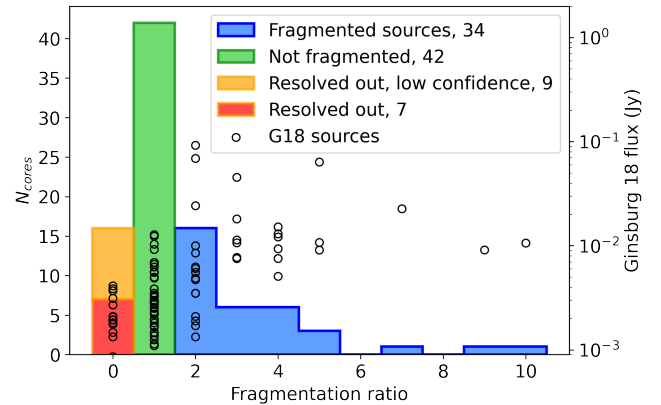


Figure 14. Number of sources from our data that fall within $1.5 \times \text{FWHM}$ of G18 sources. Over 50% of the G18 sources fragment into two or more sources. The black circles show the relationship between the flux and the fragmentation ratio of G18 sources. The left-most bin shows sources from G18 that do not have a counterpart in our data. On average, each G18 source fragments into two.

5. SUMMARY

We presented ~ 700 AU follow-up continuum observations of a massive molecular cloud in the CMZ – Sagittarius B2. We detected 425 unique

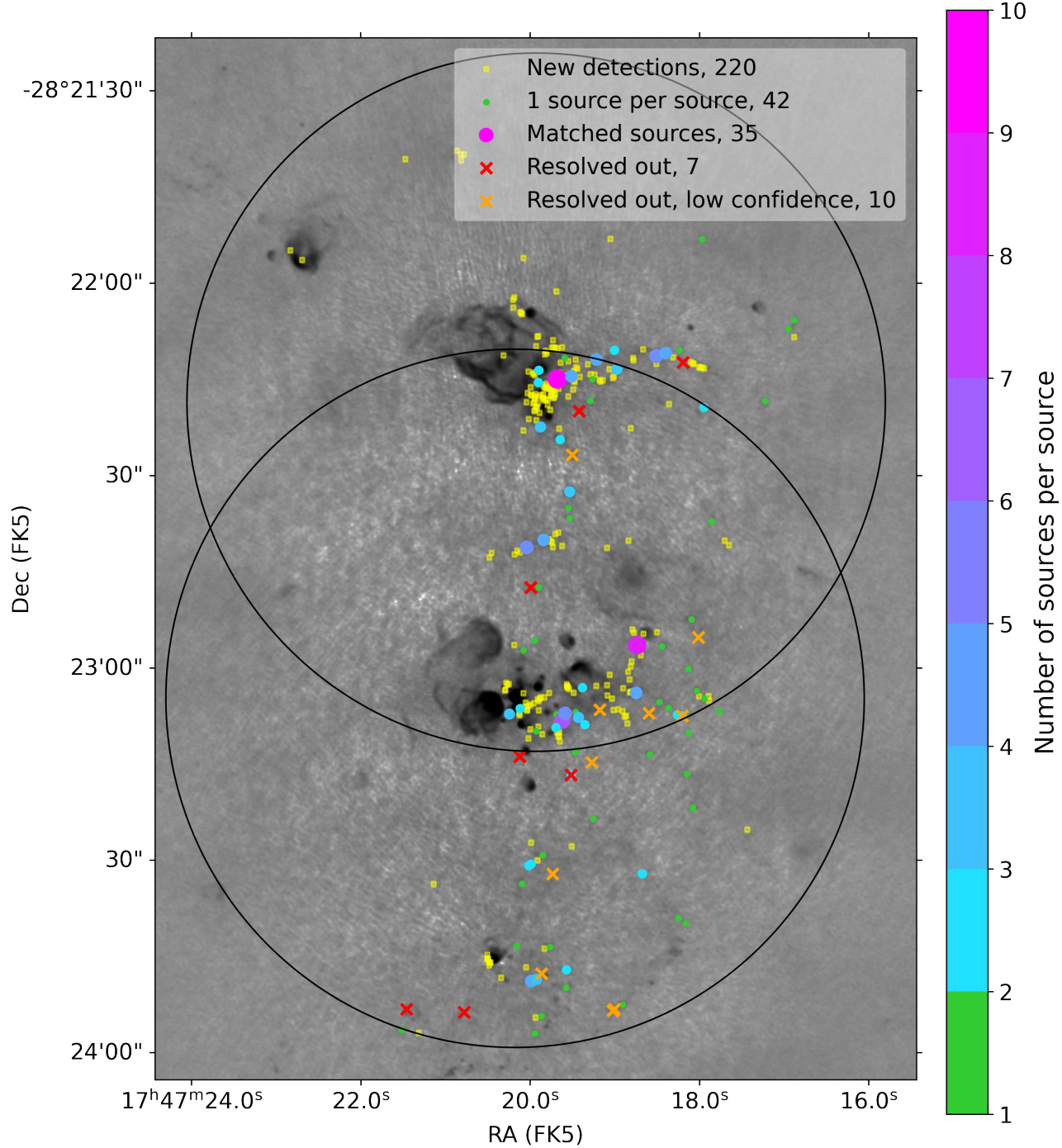


Figure 15. 3 mm ALMA mosaic of Sgr B2 adapted from [Ginsburg et al. \(2018\)](#). The black circles show the field of view of the two 3 mm pointings in this work. The filled-in circles show the sources that have been matched by-hand between the two data sets, with H II regions disregarded. The color and the size of the circles show the number of higher-resolution sources within $1.5 \times \text{FWHM}$ of the lower resolution beam, which we interpret as fragmentation. The x's indicate sources resolved out with the increase in resolution and increase in the shortest baseline length. “Low confidence” detections from [Ginsburg et al. \(2018\)](#) are shown in orange. The detections visible in the figure but not marked are either H II regions or are located at the edge of the high-resolution pointings where the sensitivity was below the detection threshold for such sources. Some of the “resolved out” sources (including the red high-confidence detections) are likely to be false detections caused by imaging artifacts.

cores: 371 at 3 mm, a twofold increase compared to [Ginsburg et al. \(2018\)](#), and 222 at 1 mm. Most of the newly detected sources are due to the increased sensitivity, while about a fifth come from resolving fragmented sources. We find most sources to be marginally resolved and have a spectral index consistent with $2 < \alpha \lesssim 3$. We infer that the dusty objects we observe must be warmer than disks observed in the Galaxy. Because of their high temperatures, these sources are unlikely to be prestellar cores. Because of their high column densities, they are unlikely to be Stage II or later YSOs. We therefore conclude that the sample is comprised primarily of Stage 0/I YSOs. Using direct source counting, we infer the total stellar mass of $2300 M_{\odot}$ for Sgr B2 N and $6300 M_{\odot}$ for Sgr B2 M. The resulting star formation rate is $0.0031 M_{\odot} \text{ yr}^{-1}$ for Sgr B2 N and $0.0085 M_{\odot} \text{ yr}^{-1}$ for Sgr B2 M.

ACKNOWLEDGMENTS

This paper makes use of the following ALMA data: ADS/JAO.ALMA#2016.1.00550.S, ADS/JAO.ALMA#2013.1.00269.S. ALMA is a partnership of ESO (representing its mem-

ber states), NSF (USA) and NINS (Japan), together with NRC (Canada), MOST and ASIAA (Taiwan), and KASI (Republic of Korea), in cooperation with the Republic of Chile. The Joint ALMA Observatory is operated by ESO, AUI/NRAO and NAOJ. The National Radio Astronomy Observatory is a facility of the National Science Foundation operated under cooperative agreement by Associated Universities, Inc. AG acknowledges support from the NSF under CAREER 2142300 and AST 2008101 and 2206511. NB and DJ were supported by NRAO Student Observing Support grants SOSPA8-010 and SOSPA6-026.

Facilities: ALMA

Software: Image reduction and final catalogs are available on GitHub: https://github.com/bazarsen/SgrB2_ALMA_continuum. This work utilized the following tools: `astropy` ([Astropy Collaboration et al. 2013, 2018](#)), `CASA` version 5.7.0-134.el7 ([McMullin et al. 2007](#)), `astrodendro` ([Rosolowsky et al. 2008](#)), `dendrocat`, `radiobeam`.

REFERENCES

- Andrews, S. M., Huang, J., Pérez, L. M., et al. 2018, ApJL, 869, L41, doi: [10.3847/2041-8213/aaf741](https://doi.org/10.3847/2041-8213/aaf741)
- Astropy Collaboration, Robitaille, T. P., Tollerud, E. J., et al. 2013, A&A, 558, A33, doi: [10.1051/0004-6361/201322068](https://doi.org/10.1051/0004-6361/201322068)
- Astropy Collaboration, Price-Whelan, A. M., Sipőcz, B. M., et al. 2018, AJ, 156, 123, doi: [10.3847/1538-3881/aabc4f](https://doi.org/10.3847/1538-3881/aabc4f)
- Barnes, A. T., Longmore, S. N., Battersby, C., et al. 2017, MNRAS, 469, 2263, doi: [10.1093/mnras/stx941](https://doi.org/10.1093/mnras/stx941)
- Bonfand, M., Belloche, A., Garrod, R. T., et al. 2019, A&A, 628, A27, doi: [10.1051/0004-6361/201935523](https://doi.org/10.1051/0004-6361/201935523)
- Caselli, P., Pineda, J. E., Sipilä, O., et al. 2022, ApJ, 929, 13, doi: [10.3847/1538-4357/ac5913](https://doi.org/10.3847/1538-4357/ac5913)
- De Pree, C. G., Goss, W. M., & Gaume, R. A. 1998, ApJ, 500, 847, doi: [10.1086/305782](https://doi.org/10.1086/305782)
- Eisner, J. A., Arce, H. G., Ballering, N. P., et al. 2018, ApJ, 860, 77, doi: [10.3847/1538-4357/aac3e2](https://doi.org/10.3847/1538-4357/aac3e2)
- Etxaluze, M., Goicoechea, J. R., Cernicharo, J., et al. 2013, A&A, 556, A137, doi: [10.1051/0004-6361/201321258](https://doi.org/10.1051/0004-6361/201321258)
- Gallego-Calvente, A. T., Schödel, R., Alberdi, A., et al. 2022, A&A, 664, A49, doi: [10.1051/0004-6361/202141895](https://doi.org/10.1051/0004-6361/202141895)
- Ginsburg, A., & Kruijssen, J. M. D. 2018, ApJL, 864, L17, doi: [10.3847/2041-8213/aada89](https://doi.org/10.3847/2041-8213/aada89)
- Ginsburg, A., Henkel, C., Ao, Y., et al. 2016, A&A, 586, A50, doi: [10.1051/0004-6361/201526100](https://doi.org/10.1051/0004-6361/201526100)

- 1089 Ginsburg, A., Bally, J., Barnes, A., et al. 2018,
 1090 ApJ, 853, 171, doi: [10.3847/1538-4357/aaa6d4](https://doi.org/10.3847/1538-4357/aaa6d4)
- 1091 Goldsmith, P. F., Lis, D. C., Hills, R., & Lasenby,
 1092 J. 1990, ApJ, 350, 186, doi: [10.1086/168372](https://doi.org/10.1086/168372)
- 1093 GRAVITY Collaboration, Abuter, R., Amorim,
 1094 A., et al. 2018, A&A, 615, L15,
 1095 doi: [10.1051/0004-6361/201833718](https://doi.org/10.1051/0004-6361/201833718)
- 1096 Henshaw, J. D., Longmore, S. N., Kruijssen,
 1097 J. M. D., et al. 2016, MNRAS, 457, 2675,
 1098 doi: [10.1093/mnras/stw121](https://doi.org/10.1093/mnras/stw121)
- 1099 Hosek, Matthew W., Lu, J. R., Anderson, J.,
 1100 et al. 2019, ApJ, 870, 44,
 1101 doi: [10.3847/1538-4357/aaef90](https://doi.org/10.3847/1538-4357/aaef90)
- 1102 Krieger, N., Ott, J., Beuther, H., et al. 2017, ApJ,
 1103 850, 77, doi: [10.3847/1538-4357/aa951c](https://doi.org/10.3847/1538-4357/aa951c)
- 1104 Kroupa, P. 2001, MNRAS, 322, 231,
 1105 doi: [10.1046/j.1365-8711.2001.04022.x](https://doi.org/10.1046/j.1365-8711.2001.04022.x)
- 1106 Kruijssen, J. M. D., Dale, J. E., & Longmore,
 1107 S. N. 2015, MNRAS, 447, 1059,
 1108 doi: [10.1093/mnras/stu2526](https://doi.org/10.1093/mnras/stu2526)
- 1109 Lada, C. J., & Lada, E. A. 2003, ARA&A, 41, 57,
 1110 doi: [10.1146/annurev.astro.41.011802.094844](https://doi.org/10.1146/annurev.astro.41.011802.094844)
- 1111 Madau, P., & Dickinson, M. 2014, ARA&A, 52,
 1112 415, doi: [10.1146/annurev-astro-081811-125615](https://doi.org/10.1146/annurev-astro-081811-125615)
- 1113 McMullin, J. P., Waters, B., Schiebel, D., Young,
 1114 W., & Golap, K. 2007, in Astronomical Society
 1115 of the Pacific Conference Series, Vol. 376,
 1116 Astronomical Data Analysis Software and
 1117 Systems XVI, ed. R. A. Shaw, F. Hill, & D. J.
 1118 Bell, 127
- 1119 Meng, F., Sánchez-Monge, Á., Schilke, P., et al.
 1120 2022, A&A, 666, A31,
 1121 doi: [10.1051/0004-6361/202243674](https://doi.org/10.1051/0004-6361/202243674)
- 1122 Mills, E. A. C., Ginsburg, A., Clements, A. R.,
 1123 et al. 2018, ApJL, 869, L14,
 1124 doi: [10.3847/2041-8213/aaf237](https://doi.org/10.3847/2041-8213/aaf237)
- 1125 Myers, P. C., Hatchfield, H. P., & Battersby, C.
 1126 2022, ApJ, 929, 34,
 1127 doi: [10.3847/1538-4357/ac5906](https://doi.org/10.3847/1538-4357/ac5906)
- 1128 Ossenkopf, V., & Henning, T. 1994, A&A, 291,
 1129 943
- 1130 Otter, J., Ginsburg, A., Ballering, N. P., et al.
 1131 2021, ApJ, 923, 221,
 1132 doi: [10.3847/1538-4357/ac29c2](https://doi.org/10.3847/1538-4357/ac29c2)
- 1133 Richards, A. M. S., Moravec, E., Etoka, S., et al.
 1134 2022, arXiv e-prints, arXiv:2207.05591,
 1135 doi: [10.48550/arXiv.2207.05591](https://doi.org/10.48550/arXiv.2207.05591)
- 1136 Robitaille, T. P., Whitney, B. A., Indebetouw, R.,
 1137 Wood, K., & Denzmore, P. 2006, ApJS, 167,
 1138 256, doi: [10.1086/508424](https://doi.org/10.1086/508424)
- 1139 Rosolowsky, E. W., Pineda, J. E., Kauffmann, J.,
 1140 & Goodman, A. A. 2008, ApJ, 679, 1338,
 1141 doi: [10.1086/587685](https://doi.org/10.1086/587685)
- 1142 Sánchez-Monge, Á., Schilke, P., Schmiedeke, A.,
 1143 et al. 2017, A&A, 604, A6,
 1144 doi: [10.1051/0004-6361/201730426](https://doi.org/10.1051/0004-6361/201730426)
- 1145 Schmiedeke, A., Schilke, P., Möller, T., et al. 2016,
 1146 A&A, 588, A143,
 1147 doi: [10.1051/0004-6361/201527311](https://doi.org/10.1051/0004-6361/201527311)
- 1148 Schwörer, A., Sánchez-Monge, Á., Schilke, P.,
 1149 et al. 2019, A&A, 628, A6,
 1150 doi: [10.1051/0004-6361/201935200](https://doi.org/10.1051/0004-6361/201935200)
- 1151 Tobin, J. J., Sheehan, P. D., Megeath, S. T., et al.
 1152 2020, ApJ, 890, 130,
 1153 doi: [10.3847/1538-4357/ab6f64](https://doi.org/10.3847/1538-4357/ab6f64)
- 1154 Williams, J. P., & Cieza, L. A. 2011, ARA&A, 49,
 1155 67, doi: [10.1146/annurev-astro-081710-102548](https://doi.org/10.1146/annurev-astro-081710-102548)

APPENDIX

A. CLEANING AND SELF-CALIBRATION TESTING

Sgr B2 region is one of the most complex regions that ALMA can observe. Pointing Band 3 beam at one of the two largest cores N or M places the other of the two just on the edge of the beam, significantly contributing to the artifacts in the image. We tested different cleaning approaches with special focus on masking and choosing the right cleaning threshold.

We found that the choice of mask significantly affects the quality of the final image. Generally, it is recommended to mask the images conscientiously, only including the real emission (Richards et al. 2022). At first, we tried to use RMS-based masks. We went through the calibration process using 5σ , 3σ , and 2σ masks based on the noise in the inner, signal-free region of the image. The resulting residuals contained very sharp edges around the mask contours. We then switched to a less restrictive approach: we drew polygons around visually identifies emission regions. The resulting mask covered more emission, but also included some of the artifact-rich regions. After cleaning, the images ended up with several factors lower noise than with RMS-based masks and the residual did not have any abrupt features. To minimize the effect of including the artifacts in the cleaning mask, especially in the first few iterations where they are the most prominent, we decided to use the “strict” mask for the first two iterations and then use the more broad mask for the remainder of the cleaning and calibration process. This time, we drew two sets of masks for each pointing: one containing just the brightest emission similar to the 5σ mask, but also including significant sources of emission further away from the center of the image, and a more broad mask where polygons surround any regions with visible emission. The use of a combination of a strict and broad masks resulted in a few percent lower RMS than using only the broad mask.

Generally, we used 6σ cleaning threshold for the first two cleaning iterations and 3σ for the remainder of the cleaning and calibration. However, the Band 6 pointing of Sgr B2 N suffered from divergence at these thresholds. Using higher-threshold cleaning, we determined that the image significantly improves after amplitude and phase calibration. After testing different cleaning thresholds, we found that the deepest we can clean the image without the clean diverging is $\sim 10\sigma$ until the amplitude and phase calibration and then the 3σ cleans will not diverge. The lowest measured RMS for each pointing is presented in Table 3. The self-calibration progress images highlighting different regions are shown in Figure 16.

A.1. *Evaluation using unsharp masking*

We attempted to use unsharp masking to evaluate at what value lowering cleaning threshold no longer improves the image on small scales. To create a sharpened image, the original image is first smoothed using a Gaussian kernel. Smoothing removes “blurs” small scale structures effectively removing them while keeping the large scale structures mostly intact. Different size of the smoothing kernel can be chosen to effect different size-scales. Typically, the sharpened image is:

$$\text{Sharpened} = \text{Original} \times A - \text{Smoothed} \times (A - 1), \quad (\text{A1})$$

where A determines how strong the effect is.

Table 3. Lowest RMS within the inner, signal-free region of each pointing during different calibration stages. The cleaning thresholds for the first two cleaning iterations were $\sim 6\sigma$ and $\sim 3\sigma$ for the remainder of the self-calibration process. The last two columns show the source extraction threshold values within the inner 40% and 90% of the imaged area. The noise was calculated within the concentric annuli described in Section 3.1.

Pointing	Uncalibrated	Phase, inf	Phase, int	Phase+amp, inf	Phase+amp, 15s	4σ -40% $_{image}$	4σ -90% $_{image}$
	mJy	mJy	mJy	mJy	mJy	mJy	mJy
N, 3 mm	0.047	0.044	0.032	—	—	0.13	0.43
M, 3 mm	0.105	0.068	0.054	0.051	—	0.20	0.61
N, 1 mm	1.37	1.35	1.35	0.47	0.35	1.41	4.62
M, 1 mm	0.55	0.40	0.30	0.25	—	1.00	3.27

Generally, cleaning to a lower threshold results in “better” images. However, cleaning too deep results in the `tclean` model including artifacts. In highly complex, high-dynamic-range images some of the artifacts will be present in the model unless an extremely shallow clean is performed. We strove to achieve a balance between cleaning depth and the amount of artifacts in the image model. We found that decreasing the cleaning threshold always decreases the measured RMS, which consequently could not be used to determine the “best” cleaning threshold.

The majority of the artifacts in our images are small-scale: concentric rings and radial streaks with scale-length smaller than the beam size. We used a simplified version of unsharp masking, Sharpened = Original – Smoothed, to create large-scale-structure-free versions of our images at different cleaning thresholds. If there exists a cleaning threshold at which small-scale artifacts are no longer removed by cleaning, we should be able to detect it by measuring the RMS of these sharpened images. However, we found no such correlation and the measured noise in sharpened images steadily decreased with the cleaning depth.

During the unsharp masking investigation we made sharpened versions of the final images. Upon inspection, we identified a core-like source close to Sgr B2 S HII region as shown in Figure 17. Because of the core’s proximity to the bright HII region, the chosen source extraction parameters are not able to identify it as a separate source. Thus, this source is not included in our final catalog. While unsharp masking is a viable method to identify such otherwise “hidden” sources, the sharpened images cannot be used for data analysis as the flux is not conserved during the transformation.

B. SOURCE CATALOG

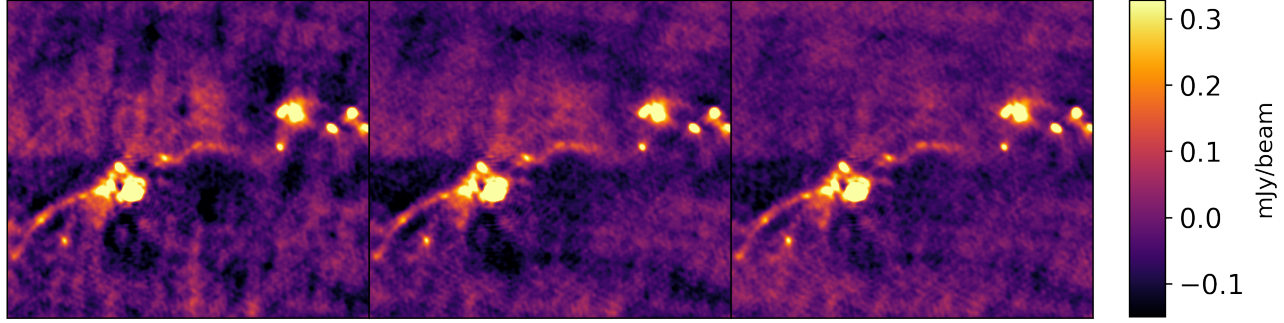
We present an excerpt from Sgr B2 N core catalog at 3 mm in Table 4. The full catalogs are available in machine-readable format and on GitHub: https://github.com/bazarsen/SgrB2_ALMA_continuum.

C. RADIAL CORE DISTRIBUTION

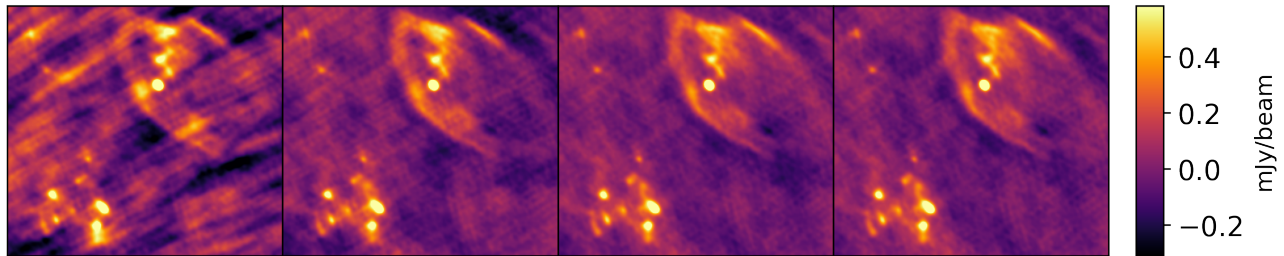
We show the core volume number density distribution as a function of distance from the center of each of the two main clusters in Figure 18. The distributions follow a power law with a slope of 2 near the center and increases to 3 at the very edges. This distribution calculation does not take into

Table 4. First 25 entries of the Sgr B2 N core catalog at 3 mm. The full catalogs for each pointing are available in machine-readable format.

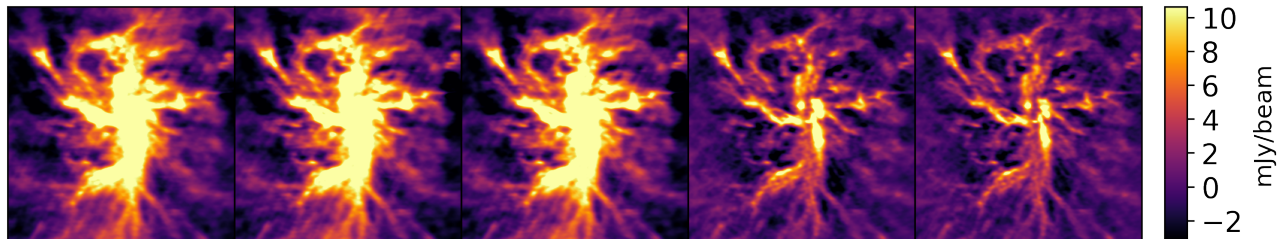
ID	$S_{\nu,flux}$ mJy	$S_{\nu,peak}$ m.Jy beam $^{-1}$	$S_{\nu,err}$ m.Jy beam $^{-1}$	FWHM $_{maj}$ $''$	FWHM $_{min}$ $''$	RA (ICRS)	Dec (ICRS)	Score	G18	T_B K	α	α_{err}	Mass M_{\odot}
1	0.71	0.43	0.032	0.115	0.071	17:47:19.884	-28:22:20.316	2	-	8	2.4	0.2	10.5
2	1.97	1.48	0.032	0.092	0.082	17:47:19.9464	-28:22:19.992	2	-	29	2.12	0.09	29.3
3	1.23	1.14	0.032	0.076	0.061	17:47:19.9368	-28:22:19.812	2	-	22	2.46	0.09	18.2
4	7.2	3.39	0.032	0.176	0.059	17:47:19.908	-28:22:19.452	1	-	68	2.02	0.04	106.9
6	1.2	1.11	0.032	0.098	0.054	17:47:19.9272	-28:22:19.272	2	-	22	2.4	0.1	17.8
8	0.67	0.47	0.032	0.105	0.072	17:47:19.9632	-28:22:18.84	2	-	9	2.2	0.3	9.9
9	0.97	0.71	0.032	0.093	0.064	17:47:19.9032	-28:22:18.804	1	-	14	2.2	0.2	14.4
11	2.45	1.66	0.032	0.115	0.078	17:47:19.9512	-28:22:18.624	2	-	33	1.3	0.2	36.3
12	0.37	0.38	0.032	0.078	0.06	17:47:20.04	-28:22:18.624	2	-	7	2.8	0.2	5.4
16	7.62	2.23	0.032	0.163	0.132	17:47:19.8072	-28:22:18.264	1	-	45	2.37	0.05	113.0
18	2.33	1.94	0.032	0.091	0.052	17:47:19.836	-28:22:18.3	2	-	39	1.78	0.09	34.6
20	1.59	1.42	0.032	0.095	0.051	17:47:19.9416	-28:22:18.012	1	-	28	1.5	0.2	23.6
22	2.96	1.83	0.032	0.105	0.067	17:47:19.8408	-28:22:18.012	2	-	36	2.28	0.06	43.8
26	0.5	1.33	0.032	0.042	0.033	17:47:19.8456	-28:22:17.904	2	-	26	2.0	0.1	7.5
27	4.61	1.54	0.032	0.271	0.063	17:47:19.9416	-28:22:17.724	1	-	31	2.14	0.08	68.4
29	0.86	0.77	0.032	0.091	0.053	17:47:19.9056	-28:22:17.76	1	-	15	2.5	0.1	12.8
31	1.27	3.0	0.032	0.062	0.025	17:47:19.98	-28:22:17.58	1	-	60	2.03	0.05	18.8
32	7.58	4.69	0.032	0.105	0.071	17:47:19.9872	-28:22:17.436	1	-	94	1.87	0.03	112.5
33	0.89	1.54	0.032	0.06	0.036	17:47:19.8744	-28:22:17.472	2	-	31	2.5	0.06	13.2
34	2.72	1.22	0.032	0.141	0.093	17:47:19.8408	-28:22:17.436	2	-	24	2.73	0.07	40.3
35	3.89	1.93	0.032	0.136	0.088	17:47:19.9392	-28:22:17.328	2	-	39	1.84	0.09	57.7
37	0.07	0.18	0.032	0.046	0.031	17:47:19.8744	-28:22:22.152	2	-	3	3.2	0.3	1.0
39	0.09	0.19	0.032	0.054	0.037	17:47:19.92	-28:22:21.432	2	-	3	3.4	0.3	1.4
40	0.56	0.28	0.032	0.115	0.078	17:47:20.0136	-28:22:21.252	1	-	5	2.7	0.3	8.3
63	0.1	0.17	0.032	0.067	0.033	17:47:19.7568	-28:22:19.848	1	-	3	3.9	0.3	1.4



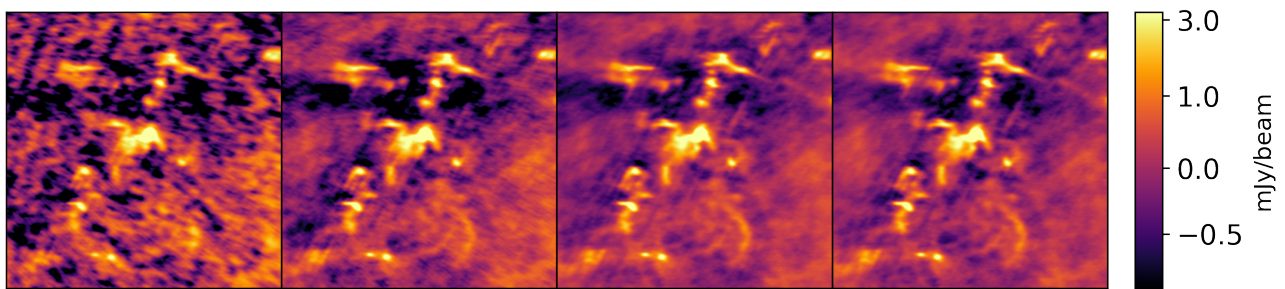
(a) Sgr B2 Z10.24 H II region and the surrounding cores from the Sgr B2 N pointing at 3 mm. The bright Sgr B2 N at the center of the pointing is causing vertical streaking in this region. The bright H II region shown in the cutout is causing concentric ring-like artifacts.



(b) Sgr B2 Y H II region and the surrounding cores from the Sgr B2 M pointing at 3 mm. The radial streaks are caused by the extremely bright source at the center of the pointing – Sgr B2 M.



(c) Sgr B2 N at 1 mm. Diagonal artifacts are mitigated throughout the self-calibration process. The first iteration of the amplitude and phase self-calibration (4th panel) shows some of the large scale flux missing due to the flagging of short baselines.



(d) A clump of sources South-East of Sgr B2 M at 1 mm.

Figure 16. A sample of zoom-ins for each pointing at different calibration stages highlighting different types of artifacts. The most prominent artifacts, concentric rings and radial streaks, are caused by the extremely bright sources in the field-of-view. The iterations from left to right, if present, are: uncalibrated, phase, `solint = inf`; phase, `solint = int`; phase and amplitude, `solint = inf`; phase and amplitude, `solint = int`.

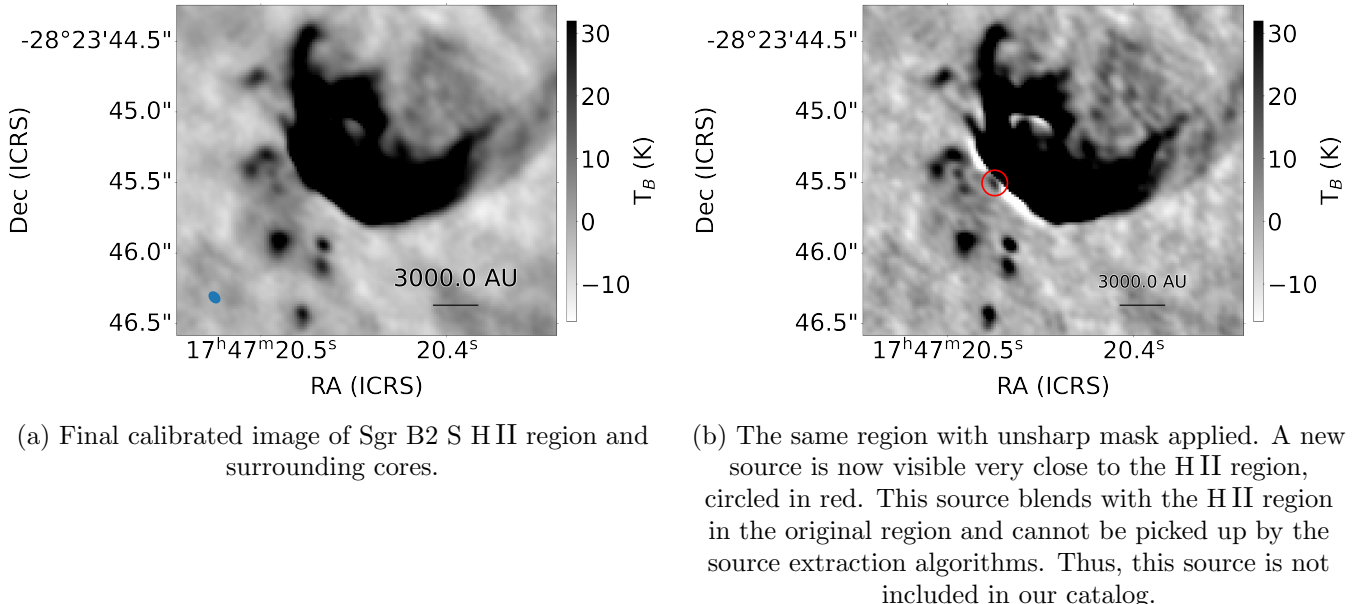


Figure 17. Unsharp masking revealing a source very close to a bright H II region.

account the radial decrease in sensitivity of our data, thus the core number density at large distances is underestimated. A sudden increase in the core number density for Sgr B2 M at 7×10^4 AU is caused by a large number of sources in the vicinity of Sgr B2 South.

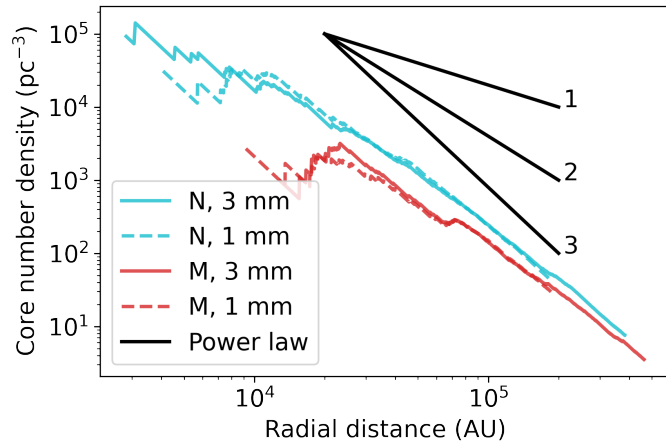


Figure 18. Radial core distribution as a function of number density. Several power law slopes are overplotted. The slope of the core distribution varies from ~ 2 near the center of the clusters to ~ 3 at the edges. The small bump at 7×10^4 AU for Sgr B2 M is due to a large number of cores around Sgr B2 South.

1224

1225